A Dissertation

entitled

Radiative Cooling in Disks and its Effects on the Formation of Giant Planets via the Gravitational Instability

by

David J. Nero

Submitted to the Graduate Faculty as partial fulfillment of the requirements for the Doctor of Philosophy Degree in Physics

Dr. Jon Bjorkman, Committee Chair

Dr. Lawrence Anderson-Huang, Committee Member

Dr. Lee Hartmann, Committee Member

Dr. Victor Karpov, Committee Member

Dr. S. Thomas Megeath, Committee Member

Dr. Adolf Witt, Committee Member

Dr. Patricia R. Komuniecki, Dean
College of Graduate Studies

The University of Toledo

August 2010

An Abstract of

Radiative Cooling in Disks and its Effects on the Formation of Giant Planets via the Gravitational Instability

by

David J. Nero

Submitted to the Graduate Faculty as partial fulfillment of the requirements for the Doctor of Philosophy Degree in Physics

The University of Toledo
August 2010

The gravitational instability provides a means of rapidly forming giant planets with large orbital radii. For protoplanetary disks to be unstable to gravitational fragmentation, they must 1) have a Toomre $Q \lesssim 1$ and 2) be able to cool the excess energy from a collapsing perturbation in less than the dynamical time ($\Omega t_{\rm cool} \lesssim 1$). We present an analytical technique for calculating this perturbation cooling time for externally illuminated disks and/or disks with internal heating. We compare our analytical technique with a numerical Monte Carlo code, and find good agreement.

We use our analytical technique to test the ability of the gravitational instability to re-create the observed planetary systems of Fomalhaut, HR 8799, and HL Tau. We find that the required mass interior to the planet's orbital radius is $\sim 0.1\ M_{\odot}$ for Fomalhaut b, the protoplanet orbiting HL Tau, and the outermost planet of HR 8799. The two inner planets of HR 8799 probably could not have formed *in situ* by disk fragmentation.

The perturbation cooling time can be reduced significantly through the inclusion of geometrical effects, specifically fragmentation originating at a location other than the disk mid-plane, and/or dust settling. In particular, dust settling to one-tenth of the gas scale height can reduce the perturbation cooling below the fragmentation threshold for all surface densities $\Sigma \lesssim 10^3$ g/cm^2.

We study the fragmentation criteria and fragment masses produced for a grid of parameters covering protostellar masses ranging from 0.1–5 $M_{\odot}$, ages ranging from 0.5–10 Myr, and differing degrees of dust settling. We find that the instability criteria and fragment mass scales with protostellar mass (as expected), while the protostellar age (i.e., luminosity) provides only a modest effect—indicating that disk fragmentation is equally likely at all stages of protostellar evolution, given sufficiently high disk mass. Dust settling can lead to disk fragmentation at orbital radii that are an order of magnitude smaller than in the unsettled case.

Acknowledgments

I'd like to thank everyone who made this dissertation possible. First, I'd like to thank my adviser, Dr. Jon Bjorkman, for sharing his infinite wisdom in radiative transfer. The countless hours (months?) spent in Jon's office have taught me that all problems can be solved through the use of a dry erase board. I'd also like to thank my other local Ph.D. committee members: Dr. Lawrence Anderson-Huang, Dr. Victor Karpov, Dr. Tom Megeath, and Dr. Adolf Witt, for their helpful comments and constructive criticism during my annual review meetings. Special thanks goes to my external committee member, Dr. Lee Hartmann, for both helpful comments, and for making the trip from Michigan to be present for my defense.

Next, I'd like to thank the faculty, staff, and my peers at the University of Toledo Department of Physics and Astronomy. The support and friendships of the people in this department have meant a lot to me over these six years. Special thanks to some of my former and current office-mates: Erin Hardy, Erica Hesselbach, Noel Richardson, Jason Stoke, and Josh Thomas who have kept me pleasantly distracted and sane.

Finally, and most importantly, I'd like to thank my family for their support and encouragement. I'd like to express my most heartfelt gratitude and love for my wife, Calley, who followed me to Toledo so that I could be an Astrophysicist when I grow up.

Contents

List of Tables

List of Figures

Chapter 1

Introduction

As more extrasolar planets are discovered, we are increasingly pressed to describe how planets can form in such a variety of environments. Until just recently, observational selection biases have resulted in the fact that all observed extrasolar planets have been found to orbit within a few AU of their star (Butler et al., 2006). Since it seems unlikely that these planets could have formed *in situ* (Mayor & Queloz, 1995), planet migration is usually invoked (Alibert et al., 2005). Unfortunately, this means that little is known about where—and hence how—these planets originally formed.

Recently, the technique of direct-imaging has begun to present us with a new set of extrasolar planets that lie far from their star (Kalas et al., 2008; Marois et al., 2008; Greaves et al., 2008). Like previous techniques, direct imaging preferentially detects giant planets of several Jupiter masses. Furthermore, planet migration need not be invoked to explain how these planets could form at their observed locations.

The goal of this dissertation is to evaluate the efficacy of the gravitational instability at forming giant planets with large orbital separation from their star. To that end, we focus on the issue of radiative cooling, which is a key criterion for the fragmentation of a gravitationally unstable disk.

1.1 Planet Formation

One possible mechanism for giant planet formation is core accretion followed by rapid gas accretion (Pollack et al., 1996; Inaba et al., 2003). In this mechanism, planets begin their lives as micron-sized dust grains. During collisions, these grains can stick together. Initially, the aggregate growth of grains depends on dipole-dipole attraction, along with compaction.

Once these particles reach sizes of 10 cm, their fate becomes less clear. Experimental work has shown that particle collisions begin to lead to severe fragmentation once particle sizes reaches ~ 10 cm (Blum & Wurm, 2008). Furthermore, meter-sized objects are expected to experience significant gas drag, leading to rapid accretion onto the central star. Nonetheless, assuming sufficient size is reached (approximately 10 m), these planetesimals decouple from the gas, and begin to efficiently sweep up material. If a planetesimal is able to accrete enough mass (typically in the form of ices), it begins to rapidly capture gas, ultimately becoming a gas giant planet. Less massive objects become asteroids, comets, terrestrial planets, or dwarf planets, while massive gas-starved objects become either ice giants or "super earths".

While ideal for explaining "small" objects ranging from asteroids to terrestrial planets, the core accretion mechanism has difficulty forming giant planets at large radii. The primary reason for this is that the initial core accretion time scales as r^3, where r is the orbital radius of the planet (Ikoma et al., 2000; Kenyon & Bromley, 2008). Thus, while it may take ~ 1 Myr to form a gas giant at 5 AU via core accretion, it would take ~ 1 Gyr for the same process at 50 AU—far longer than the ~ 3 Myr observed lifetimes of protoplanetary disks (Haisch et al., 2001).

Another mechanism for giant planet formation is disk fragmentation as a consequence of the gravitational instability (Kuiper, 1951; Cameron, 1978; Boss, 1997, see also the recent review by Durisen et al. 2007 and Stamatellos & Whitworth 2009 for recent developments). Provided that the disk surface density is sufficiently large, this

mechanism can form giant planetary embryos on time scales of a few orbital periods. However, if the surface density is too large, the disk is unable to cool sufficiently fast for fragmentation to take place at all (Rafikov, 2005). The combination of these requirements implies gravitational instability can only form massive planets at large radii.

1.2 Disk Fragmentation

In order to be unstable to fragmentation, a disk first needs to have a large enough surface density to be gravitationally unstable (Toomre, 1964). Such a disk will develop spiral density waves. If in addition to this first requirement, there also exist locations in the disk where the radiative cooling timescale is shorter than the dynamical timescale, the spiral density waves can proceed to collapse, leading to fragmentation of the disk (Gammie, 2001; Rice et al., 2003; Rafikov, 2005).

The gravitational stability of a thin, Keplerian disk is described by the Toomre (1964) Q parameter

$$Q = \frac{c_s \Omega}{\pi G \Sigma} \ , \tag{1.1}$$

where c_s is the isothermal sound speed, $\Omega = \sqrt{GM_\star/r^3}$ is the Keplerian frequency, and Σ is the surface density. The disk becomes gravitationally unstable for $Q \lesssim 1$.

While the Toomre Q is relatively straight-forward to evaluate for a given disk, the cooling constraint is somewhat more complex. From a timescale argument, a disk can fragment if the cooling time is shorter than the dynamical time:

$$\Omega t_{\rm cool} \lesssim 1 \ . \tag{1.2}$$

At issue is that there are arguably two different cooling timescales. The first controls the onset and initial growth of fragmenting gravitational instabilities. We call

this timescale the *perturbation cooling time*, since it represents the disk's efficiency at shedding excess internal energy. The second cooling timescale governs the subsequent evolution of any produced fragments, and represents the time it would take for a disk to radiate away all of its current internal energy. We call this second timescale the *total cooling time*.

We wish to stress, however, that in a purely numerical approach (i.e., a hydrodynamical simulation), this distinction between perturbation and total cooling times is a somewhat arbitrary choice, since either can be used to parametrize the radiative cooling term in the fluid energy equation. Nonetheless, an analytic study of the perturbation cooling time gives us insight into the dominant physical processes that influence the onset of disk fragmentation.

The remainder of this dissertation is organized as follows. In Chapter 2, we develop an analytic approximation for the perturbation cooling time for a circumstellar disk. In Chapter 3, we compare our analytic approximation with a numerical Monte Carlo code. In Chapter 4, we apply our technique for calculating perturbation cooling times to the planetary systems of Fomalhaut, HR 8799, and HL Tau[1] to derive the required disk mass to form these planets. We also calculate fragment masses expected to result from disk fragmentation and compare with the observed masses of these planets. In Chapter 5, we extend our cooling time calculations to include the effects of vertically displaced perturbations (e.g., arising from fragmentation along an inclined orbit), along with the effects of dust settling. In Chapter 6, we further explore the consequences of dust settling by finding the instability criteria and expected fragment masses for a range of stellar masses, ages, and different degrees of dust settling. We summarize our results in Chapter 7. In Appendix A, we present the detailed mathematics of our iterative method for solving the boundary conditions described

[1]At the time of writing, there is still some debate concerning whether HL Tau b is actually a background object.

in Chapters 2 and 5. In Appendix B, we provide analytic solutions for selected integrals of exponential integrals needed in Appendix A.

Chapter 2

Perturbation Cooling Time

In thermal equilibrium, the temperature of a circumstellar disk is set by balancing the local heating rate (incident stellar radiation plus viscous energy generation) with the cooling rate (thermal emission). If the heating term is locally perturbed, e.g. from energy released during the collapse of a point-like, self-gravitating clump, then the temperature of the disk rises by an amount ΔT. The timescale for the system to return to thermal equilibrium is

$$t_{\rm cool} = \frac{\Delta E}{\Delta L} \ , \tag{2.1}$$

where $t_{\rm cool}$ is the local perturbation cooling time, and ΔE and ΔL are the excess internal energy and luminosity, respectively. Both ΔE and ΔL arise as a result of the temperature perturbation ΔT. In contrast, the total cooling time $t_{\rm cool}^{\rm tot} = E^{\rm tot}/L^{\rm tot}$ is the timescale for the system to dissipate *all* of its internal energy. Note that unlike the total cooling time, the perturbation cooling time automatically accounts for the heating effects of external illumination.

In the thin disk approximation, cooling can only occur through the top and bottom surfaces of the disk. Thus, for a given radius, we can treat the disk as a 1-D plane-

parallel atmosphere. More explicitly,

$$t_{\rm cool} = \frac{\Delta\mathcal{E}}{8\pi\Delta H_0} \ , \tag{2.2}$$

where $\Delta\mathcal{E}$ is the excess internal energy per unit surface area, and $\Delta H_0 \equiv ({\rm d}\Delta L/{\rm d}A)/8\pi$ is the excess Eddington flux at the disk surface. Writing $\Delta\mathcal{E}$ in terms of ΔT,

$$t_{\rm cool} = \frac{1}{8\pi\Delta H_0}\left(\frac{1}{\gamma-1}\right)\frac{k_B}{\mu m_H}\int_{-\tau_0}^{\tau_0}\frac{\Delta T}{\chi}{\rm d}\tau \ , \tag{2.3}$$

where k_B is Boltzmann's constant, γ and μ are the adiabatic constant and mean molecular weight of the gas, m_H is the mass of atomic Hydrogen, χ is the mean opacity (absorption plus scattering), τ is the vertical optical depth coordinate, and τ_0 and $-\tau_0$ are the values of τ at the top and bottom surfaces of the disk, respectively. Note that we place $\tau = 0$ at the disk mid-plane rather than at the top surface. Consequently, the total optical depth of the disk is $2\tau_0$.

We write the temperature perturbation ΔT in terms of the frequency-integrated Planck function B and its perturbation ΔB,

$$\Delta T = \frac{1}{4}\frac{\pi}{\sigma T_m^3}\left(\frac{B}{B_m}\right)^{-3/4}\Delta B \ , \tag{2.4}$$

where T_m and B_m are the temperature and Planck function at the disk mid-plane. Substituting this into Equation (2.3), we obtain

$$t_{\rm cool} = \frac{1}{16}\frac{c_{\rm m}^2}{\gamma-1}\frac{1}{\sigma T_{\rm m}^4}\frac{1}{\chi}\int_0^{\tau_0}\left(\frac{B}{B_m}\right)^{-3/4}\frac{\Delta B}{\Delta H_0}\,{\rm d}\tau \ , \tag{2.5}$$

where $c_m = \sqrt{(k_B T_m)/(\mu_g m_H)}$ is the isothermal sound speed at the disk mid-plane. In addition, we make the simplifying assumption that χ is independent of depth, and is consequently well characterized by the mid-plane value. This is a good assump-

tion when self-heating is small and the disk is approximately vertically isothermal. However, when self-heating dominates (i.e., when there is a large vertical temperature gradient), this assumption may begin to break down. This issue is further investigated in Chapter 3. To find B and ΔB, we solve the equations of radiative transfer.

2.1 Radiative Transfer

In order to account for the absorption and reprocessing of external radiation, along with viscous energy generation, we need to consider a minimum of two frequency ranges. *External* corresponds to radiation emitted from the star and absorbed or scattered by the disk. *Diffuse* corresponds to radiation emitted by the disk as a result of viscous energy generation or by re-emission of absorbed *external* radiation. For simplicity, we assume gray opacity (i.e., the appropriate mean for both the *external* and *diffuse* radiation) and negligible thermal emission from the disk at the *external* frequencies (i.e., the star and disk are at significantly different temperatures). Since the transfer equation is linear, we can split it into two pieces.

$$\mu \frac{dI^{\rm ext}}{d\tau^{\rm ext}} = S^{\rm ext} - I^{\rm ext} \ , \tag{2.6}$$

$$\mu \frac{dI^{\rm diff}}{d\tau^{\rm diff}} = S^{\rm diff} - I^{\rm diff} \ , \tag{2.7}$$

where here μ is the cosine of the angle between the propagation direction and the unit normal to the disk surface, and $I^{\rm ext}$ and $I^{\rm diff}$ are the mean intensities for the *external* and *diffuse* radiation, respectively. Note that the optical depth coordinates $\tau^{\rm ext}$ and $\tau^{\rm diff}$ may be significantly different.

The source functions S are given by

$$S^{\rm ext} = \frac{\sigma^{\rm ext}}{\chi^{\rm ext}} J^{\rm ext} \ , \tag{2.8}$$

$$S^{\rm diff} = \frac{\sigma^{\rm diff} J^{\rm diff} + \kappa^{\rm diff} B}{\chi^{\rm diff}} \ , \tag{2.9}$$

where J is the mean intensity, and σ and κ are the scattering and absorptive opacities, respectively. We set $\sigma^{\rm ext}$ and $\kappa^{\rm ext}$ equal to the frequency-dependent scattering and absorption at the Wien peak of the star's effective temperature, and likewise, $\sigma^{\rm diff}$ and $\kappa^{\rm diff}$ are set to their values at the Wien peak of the disk's mid-plane temperature.

We choose to work in terms of the *diffuse* optical depth coordinate, so we use $\tau^{\rm ext} = (\chi^{\rm ext}/\chi^{\rm diff})\tau^{\rm diff}$ to eliminate $\tau^{\rm ext}$ in favor of $\tau^{\rm diff}$. Taking the μ-moments of the transfer Equations (2.6) and (2.7), and using the Eddington factors $f^{\rm ext} = K^{\rm ext}/J^{\rm ext}$ and $f^{\rm diff} = K^{\rm diff}/J^{\rm diff}$ to close the set of equations, we arrive at the moment equations

$$\frac{dH^{\rm ext}}{d\tau} = -\frac{\kappa^{\rm ext}}{\chi^{\rm diff}} J^{\rm ext} \ , \tag{2.10}$$

$$\frac{dJ^{\rm ext}}{d\tau} = -\frac{\chi^{\rm ext}}{\chi^{\rm diff}} \frac{H^{\rm ext}}{f^{\rm ext}} \ , \tag{2.11}$$

$$\frac{dH^{\rm diff}}{d\tau} = \frac{\kappa^{\rm diff}}{\chi^{\rm diff}} \left(B - J^{\rm diff} \right) \ , \tag{2.12}$$

$$\frac{dJ^{\rm diff}}{d\tau} = -\frac{H^{\rm diff}}{f^{\rm diff}} \ , \tag{2.13}$$

where H is the Eddington flux.

We solve the *external* radiation field using the moment Equations (2.10) and (2.11). The Eddington flux is

$$H^{\rm ext} = H_0^{\rm ext} \frac{\sinh \beta\tau}{\sinh \beta\tau_0} \ , \tag{2.14}$$

where $H_0^{\rm ext} = H^{\rm ext}(\tau_0)$, and $\beta \equiv \kappa^{\rm ext}\chi^{\rm ext}/[(\chi^{\rm diff})^2 f^{\rm ext}]$. Note that $H_0^{\rm ext}$ is the net surface flux and does not equal the incident irradiation, owing to the effects of scattering.

This difference accounts for the albedo of the disk at the *external* frequencies. The mean intensity is

$$J^{\rm ext} = -\frac{\beta\chi^{\rm diff}}{\kappa^{\rm ext}} H_0^{\rm ext} \frac{\cosh\beta\tau}{\sinh\beta\tau_0} \ . \tag{2.15}$$

The *diffuse* radiation field has three sources of energy: accretion luminosity $L_{\rm acc}$ with surface flux $H_0 = (dL_{\rm acc}/dA)/8\pi$, absorption of *external* radiation $-dH^{\rm ext}/d\tau$, and the point-source perturbation at the mid-plane $\Delta H_0\delta(\tau)$. The Eddington flux is thus

$$H^{\rm diff} = H_0\frac{\tau}{\tau_0} - H^{\rm ext} + \Delta H_0\,{\rm sgn}(\tau) \ . \tag{2.16}$$

From moment Equation (2.13), the mean intensity is

$$\begin{aligned} J^{\rm diff} &= J^{\rm diff}(\tau_0) + \frac{1}{f^{\rm diff}}\int_\tau^{\tau_0} H^{\rm diff}\,dt \\ &= H_0\left(\frac{\tau_0^2-\tau^2}{2f^{\rm diff}\tau_0} + \frac{1}{g^{\rm diff}}\right) - H_0^{\rm ext}\left(\frac{\cosh\beta\tau_0 - \cosh\beta\tau}{\beta f^{\rm diff}\sinh\beta\tau_0} + \frac{1}{g^{\rm diff}}\right) \\ &\quad +\Delta H_0\left(\frac{\tau_0-|\tau|}{f^{\rm diff}} + \frac{1}{g^{\rm diff}}\right) \ , \end{aligned} \tag{2.17}$$

where the second Eddington factor $g^{\rm diff} = H^{\rm diff}(\tau_0)/J^{\rm diff}(\tau_0)$. The condition of radiative equilibrium (moment Equation [2.12]) gives the Planck Function in terms of $H^{\rm diff}$ and $J^{\rm diff}$

$$\begin{aligned} B &= J^{\rm diff} + \frac{\chi^{\rm diff}}{\kappa^{\rm diff}}\frac{dH^{\rm diff}}{d\tau} \\ &= J^{\rm diff} + \frac{\chi^{\rm diff}}{\kappa^{\rm diff}}\frac{H_0}{\tau_0} + \frac{\kappa^{\rm ext}}{\kappa^{\rm diff}}J^{\rm ext} + 2\frac{\chi^{\rm diff}}{\kappa^{\rm diff}}\Delta H_0\delta(\tau) \ . \end{aligned} \tag{2.18}$$

Subtracting $B(\Delta H_0 = 0)$, we find the perturbation

$$\Delta B = \Delta H_0\left(\frac{\tau_0-|\tau|}{f^{\rm diff}} + \frac{1}{g^{\rm diff}} + 2\frac{\chi^{\rm diff}}{\kappa^{\rm diff}}\delta(\tau)\right) \ . \tag{2.19}$$

Plugging this result into the cooling time (eq. [2.5]), we find the expression

$$t_{\rm cool} = \frac{1}{16}\frac{c_{\rm m}^2}{\gamma-1}\frac{1}{\sigma T_{\rm m}^4}\frac{1}{\chi^{\rm diff}}\left[\int_0^{\tau_0}\left(\frac{B}{B_m}\right)^{-3/4}\left(\frac{\tau_0-\tau}{f^{\rm diff}}+\frac{1}{g^{\rm diff}}\right)d\tau+\frac{\chi^{\rm diff}}{\kappa^{\rm diff}}\right] . \quad (2.20)$$

We describe an iterative method for finding the unknown constants $f^{\rm ext}$, $H_0^{\rm ext}$, $f^{\rm diff}$, and $g^{\rm diff}$ in Appendix A.

2.2 Analytic Limits for a Vertically Isothermal Disk

If self-heating from accretion is negligible ($H_0 \ll H_0^{\rm ext}$), or if the disk is optically thin ($\tau_0 \ll 1$), then the disk is vertically isothermal, $B/B_m \to 1$, and Equation (2.20) can be integrated analytically. In the former case, there is still a temperature rise in the surface layers, but since most of the internal energy is stored in the interior of the disk, the error is minimal. The cooling time (eq. [2.20]) simplifies to

$$t_{\rm cool} = \frac{1}{16}\frac{c_{\rm m}^2}{\gamma-1}\frac{1}{\sigma T_{\rm m}^4}\left(\frac{\chi^{\rm diff}\Sigma^2}{8f^{\rm diff}}+\frac{\Sigma}{2g^{\rm diff}}+\frac{1}{\kappa^{\rm diff}}\right) . \quad (2.21)$$

The first term in parentheses dominates in the optically thick ($\tau_0 \gg 1$) limit, while the last term dominates in the optically thin ($\tau_0 \ll 1$) limit. The middle term becomes important for intermediate optical depths ($\tau_0 \sim 1$), and represents the effects of the temperature perturbation at the disk surface.

In the optically thick ($\tau_0 \gg 1$) limit, the Eddington factor $f^{\rm diff} \to 1/3$, and

$$t_{\rm cool} = \frac{3}{128}\frac{c_{\rm m}^2}{\gamma-1}\frac{1}{\sigma T_{\rm m}^4}\chi^{\rm diff}\Sigma^2 . \quad (2.22)$$

In the optically thin ($\tau_0 \ll 1$) limit, the perturbation cooling time becomes con-

stant with respect to Σ

$$t_{\rm cool} = \frac{1}{16}\frac{c_{\rm m}^2}{\gamma-1}\frac{1}{\sigma T_{\rm m}^4}\frac{1}{\kappa^{\rm diff}} \ . \tag{2.23}$$

For a given mid-plane temperature, the optically thin limit provides the shortest possible perturbation cooling time.

2.3 Self-Heated Limit

In the limit where self-heating becomes dominant ($H_0 \gg H_0^{\rm ext}$), the ratio

$$\frac{B}{B_m} \rightarrow 1 - \left(\frac{\tau}{\tau_0}\right)^2 \ , \tag{2.24}$$

where we have also made the assumption that the disk is optically thick ($\tau_0 \gg 1$), consistent with a locally high accretion rate. The optically thick, perturbation cooling time is

$$\begin{aligned} t_{\rm cool} &= \frac{1}{16}\frac{c_{\rm m}^2}{\gamma-1}\frac{1}{\sigma T_{\rm m}^4}\frac{1}{\chi^{\rm diff}}\frac{\tau_0}{f^{\rm diff}}\int_0^{\tau_0}\left(1-\frac{\tau^2}{\tau_0^2}\right)^{-3/4}\left(1-\frac{\tau}{\tau_0}\right)\,d\tau \\ &= \frac{3}{64}\frac{c_{\rm m}^2}{\gamma-1}\frac{1}{\sigma T_{\rm m}^4}\chi^{\rm diff}\Sigma^2\left[{}_2F_1\left(\frac{1}{2},\frac{3}{4};\frac{3}{2};1\right)-2\right] \\ &\approx 0.029\frac{c_{\rm m}^2}{\gamma-1}\frac{1}{\sigma T_{\rm m}^4}\chi^{\rm diff}\Sigma^2 \ , \end{aligned} \tag{2.25}$$

where ${}_2F_1$ is the hypergeometric function, and $f^{\rm diff} \rightarrow 1/3$. Note that while the explicit Σ-dependence is the same as for the vertically isothermal case, the mid-plane temperature T_m will also increase with Σ, due to an associated increase in the accretion luminosity.

We can characterize the dependence of the mid-plane temperature on the surface density explicitly in the case of quasi-steady-state α-disks (Shakura & Sunyaev, 1973).

When the viscous shear-stress (i.e., accretion) is the dominant source of heating,

$$H_0 = \frac{9}{32\pi}\alpha c_m^2 \Omega \Sigma \ , \tag{2.26}$$

where $0 < \alpha < 1$ is the parameter introduced by Shakura & Sunyaev (1973) to account for turbulent viscosity (i.e., the effective kinematic viscosity is $\nu = \alpha c_m h$, where h is the disk scale height). In the optically thick, self-heated limit, the Planck function (eq. [2.18]) at the mid-plane simplifies to

$$B_m = \frac{3}{2} H_0 \tau_0 \ , \tag{2.27}$$

which together with Equation (2.26) gives

$$\sigma T_m^4 = \frac{27}{128}\alpha c_m^2 \Omega \chi^{\rm diff} \Sigma^2 \ . \tag{2.28}$$

Substituting this result into the cooling time (eq. [2.25]) gives the behavior for large Σ:

$$t_{\rm cool} \approx \frac{0.138}{\alpha(\gamma - 1)} \frac{1}{\Omega} \ . \tag{2.29}$$

We see that the cooling time is in fact constant with Σ for large surface densities. In addition, the cooling time becomes opacity-independent in this limit, and thus the temperature of the disk becomes mostly irrelevant (excluding secondary effects on γ and possibly α).

Recall that a gravitationally unstable ($Q \lesssim 1$) disk will fragment only if $\Omega t_{\rm cool} < \xi$, where ξ is a constant of order unity. Using Equation (2.29) for $t_{\rm cool}$, we find that a high-Σ disk can fragment only if

$$\alpha > \frac{0.138}{\xi(\gamma - 1)} \ . \tag{2.30}$$

Using $\xi = 1$ and $\gamma = 1.43$, we find a typical lower limit of $\alpha > 0.32$ for fragmentation. Note that this is similar in magnitude to the Gammie (2001) result, but with a different numerical constant owing to the difference between total and perturbation cooling times. Since typical values for α are 0.01–0.1 for massive disks (Zhu et al., 2009), we conclude that extremely large surface densities are, in general, detrimental to disk fragmentation. An important caveat, however, is that if the surface density is increased to such an extent that the mid-plane temperature rises above the dust sublimation threshold, then the cooling time will begin to decrease as the interior of the disk becomes optically thin and isothermal.

Chapter 3

Monte Carlo Comparison

In order to test the validity of our analytic perturbation cooling time calculation, we compare our results to those from a 1-D, plane-parallel numerical code. The numerical code uses a Monte Carlo radiative equilibrium calculation for the surface layers ($\tau \lesssim 10$) and diffusion approximation for the interior ($\tau \gtrsim 10$), and was developed to closely match the geometry and energy sources of our analytic approximation. As in our analytic approximation, the atmosphere is externally illuminated from both sides, and self-heating from accretion is included (using eq. [2.26]). In the following comparisons, we consistently use a 0.5 $M_\odot$, 2 $R_\odot$, 4000 K star with a power-law scale height $h \propto r^{5/4}$ for the disk, with a Shakura-Sunyaev α parameter of 0.1. We assume a mean molecular weight $\mu = 2.33$ and an adiabatic gas constant of $\gamma = 1.43$. For full details on the radiative equilibrium temperature calculation used in the Monte Carlo surface layers, see Bjorkman & Wood (2001). In the cases were the vertical optical depth is sufficiently small ($\tau \lesssim 10$), the entire atmosphere is computed using Monte Carlo.

To find the perturbation cooling time numerically, we use Equation (2.3), where ΔH_0 and ΔT are found by solving for the temperature structure twice: first as a background solution, and then with a small source of internal energy added at

the mid-plane. We then subtract to find the differences. Note that this numerical method avoids the major simplifying assumptions of our analytic approximation. In particular, our analytic approximation assumes that both opacities and Eddington factors are vertically uniform, while the Monte Carlo simulation does not. We also assumed that we could reproduce the relevant radiative physics using a quasi-gray assumption with only two relevant frequencies (*external* and *diffuse*), while the Monte Carlo simulation calculates the radiation field with the full frequency dependence and anisotropic scattering by the dust.

3.1 Gray Opacity

We begin our comparison using a purely absorptive, gray opacity (with $\chi = \kappa = 1$ cm^2/g). This comparison allows us to isolate the effects of assuming vertically uniform Eddington factors. The usage of a purely absorptive atmosphere also has the advantage of simplifying the solution of the *external* radiation field considerably. In this limit $f^{\rm ext} \rightarrow \mu_\star^2$, $H_0^{\rm ext} \rightarrow H_\star/2$, and $\beta \rightarrow 1/\mu_\star$ (for details on solving for the boundary conditions $f^{\rm ext}$ and $H_0^{\rm ext}$ see Appendix A). Furthermore, since $g^{\rm diff}$ is by definition depth-independent, the only potential source of error is the depth-dependence of the *diffuse* Eddington factor $f^{\rm diff.}$

The mid-plane temperatures at 1, 10, and 100 AU are shown as a function of surface density in Figure 3-1. Note that we end the comparison at the dust sublimation temperature, since neither of our approaches were developed to account for a sudden vertical transition from dust to gas as the primary opacity source.

In general, the analytic approximation is in good agreement with the Monte Carlo (for the gray case). However, there is some slight deviation for surface densities near unity, corresponding to optical depths near unity. This is not surprising, since this is where the effect of an incorrect *diffuse* Eddington factor $f^{\rm diff}$ would be most

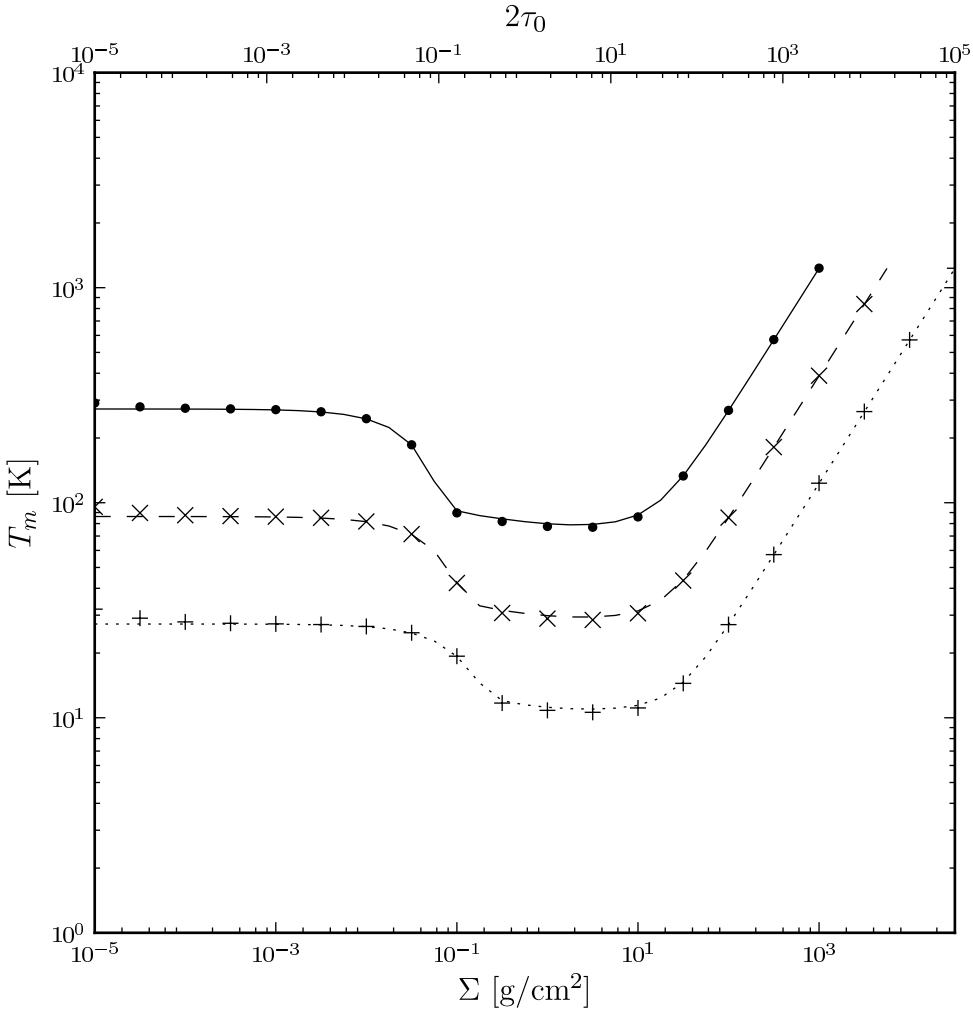

Figure 3-1: Comparison of the mid-plane temperature as a function of surface density for both our analytic approximation (lines) and full numerical calculation (points), using a purely absorptive, gray opacity with $\chi = \kappa = 1$ cm^2/g. Comparisons are made at 1 AU (solid lines and filled points), 10 AU (dashed lines and crosses), and 100 AU (dotted lines and pluses) from a 0.5 $M_\odot$, 2.0 $R_\odot$, 4000 K star.

pronounced. At these optical depths, the *external* radiation will have been completely absorbed in the surface layers, yet the disk is not yet optically thick to its own *diffuse* radiation. For smaller optical depths, the disk is dominated by the well-determined *external* radiation field, while at higher optical depths, the disk is well into the diffusion limit.

In Figure 3-2, we plot vertical slices of the disk temperature at 100 AU for surface densities of 10^{-4}, 10^{0}, and 10^{4} g/cm^2, highlighting the optically thin, intermediate, and self-heated limits, respectively. Since the *external* radiation field sets the temperature rise at the disk surface—and is well determined for the purely absorptive limit—the Monte Carlo and analytic calculations are, not surprisingly, in good agreement.

In Figure 3-3, we plot a comparison of the perturbation cooling time as calculated using our analytic approximation and Monte Carlo solution. With the exception of some disagreement for surface densities (and optical depths) near unity, both techniques for calculating the perturbation cooling time are in good agreement. The deviations near unity are caused by the somewhat inaccurate calculation of the mid-plane temperature as a result of neglecting the vertical dependence of $f^{\rm diff}$.

3.2 Non-Gray Opacity

We now extend our comparison to include the effects of a more realistic opacity model. Using the dust opacity model of Wood et al. (2002), we plot comparisons of mid-plane temperature in Figure 3-4, vertical temperature slices in Figure 3-5, and perturbation cooling time in Figure 3-6. As in the gray case, the vertical dependence of $f^{\rm diff}$ leads to inaccurate mid-plane temperatures for optical depths of order unity. To some extent, this effect is exacerbated by the vertical temperature dependence of the dust opacity (fortunately, the disk is mostly isothermal at these optical depths).

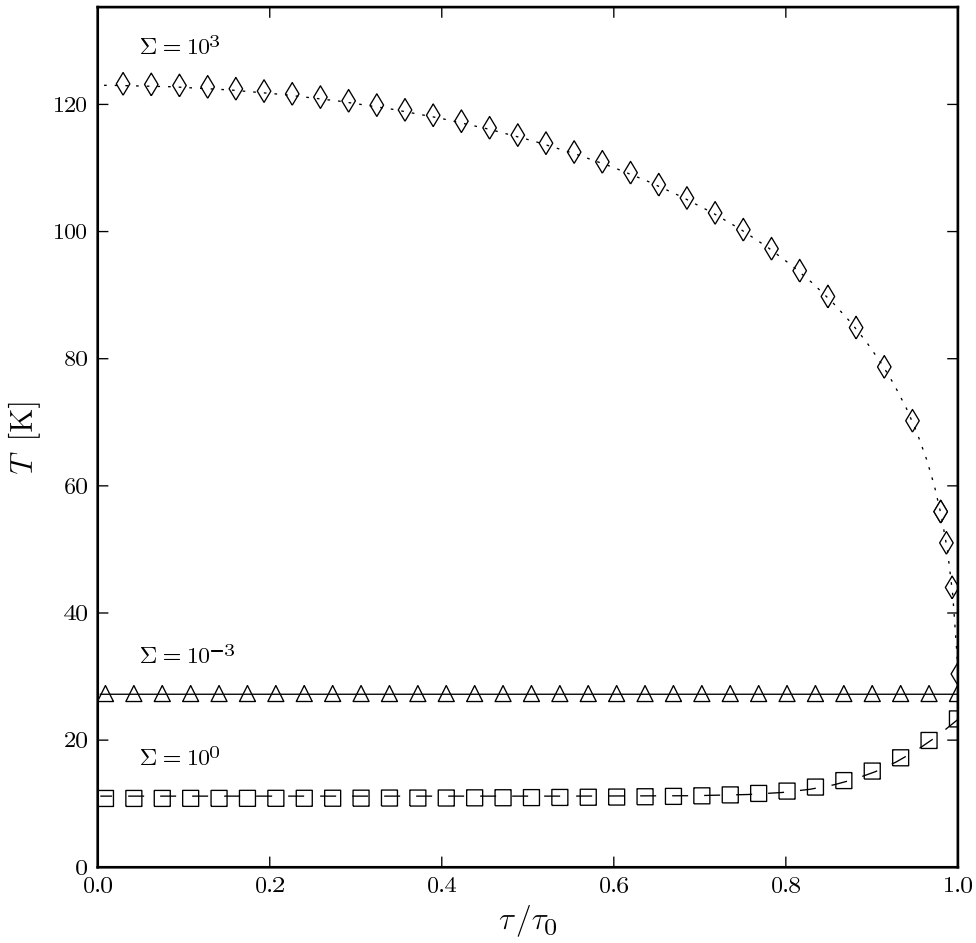

Figure 3-2: Comparison of the vertical temperature structure for both our analytic approximation (lines) and full numerical calculation (points), using a purely absorptive, gray opacity. Comparisons are made for surface densities of 10^{-3} g/cm^2 (solid lines and triangles), 10^0 g/cm^2 (dashed lines and squares), and 10^3 g/cm^2 (dotted lines and diamonds), highlighting the optically thin, intermediate, and self-heated limits, respectively. All three comparisons are made at 100 AU from a 0.5 $M_\odot$, 2.0 $R_\odot$, 4000 K star.

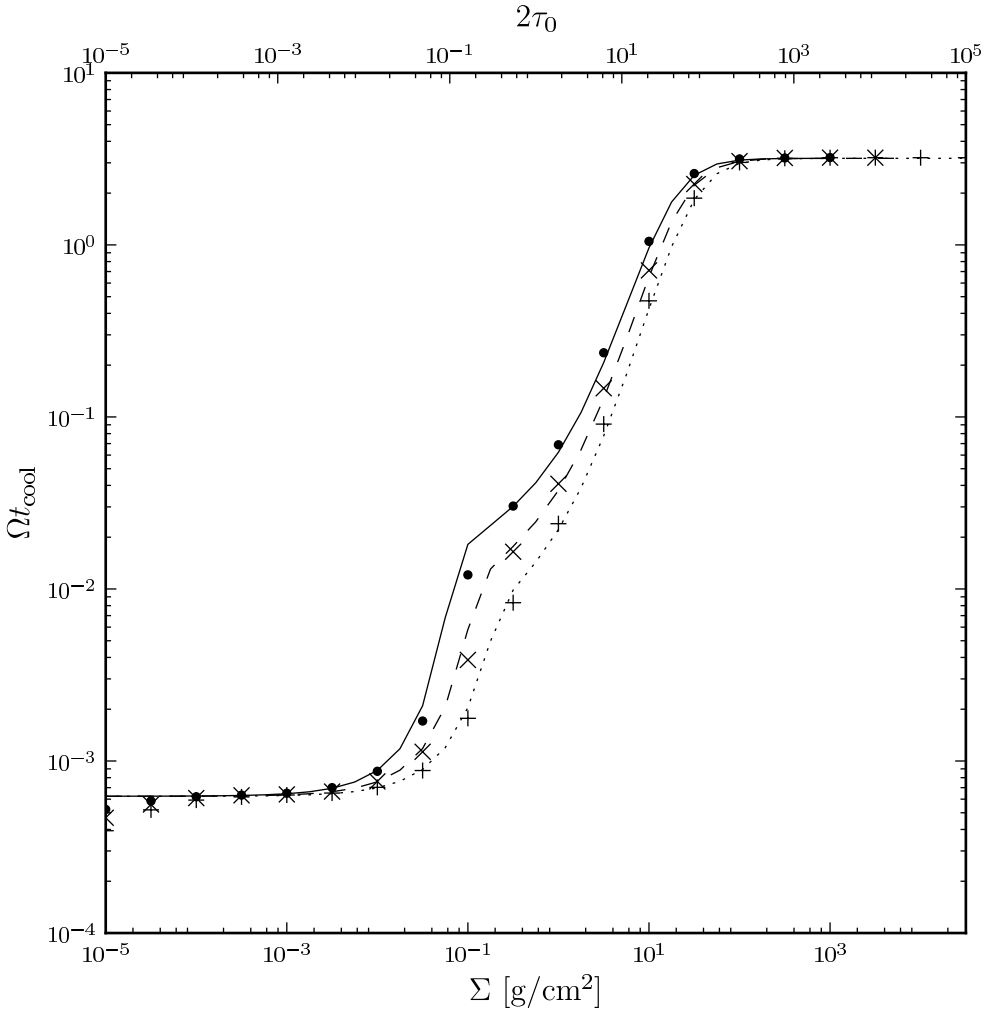

Figure 3-3: Comparison of the perturbation cooling time (normalized to the Keplerian orbital angular frequency Ω) as a function of surface density for both our analytic approximation (lines) and full numerical calculation (points), using a purely absorptive, gray opacity. Comparisons are made at 1 AU (solid lines and filled points), 10 AU (dashed lines and crosses), and 100 AU (dotted lines and pluses) from a 0.5 $M_\odot$, 2.0 $R_\odot$, 4000 K star.

Furthermore, as shown in Figure 3-5, the detailed shape of the vertical temperature structure of the disk depends on the solution to the *external* radiation field. By matching the boundary conditions for $f^{\rm ext}$ at the mid-plane, we sacrifice the accuracy of the temperature in the surface layers. This was done to improve our calculation of the mid-plane temperature, which plays a much larger role in determining $t_{\rm cool}$ than the surface effects do. Nonetheless, our analytic mid-plane temperatures can differ by up to 20% from the Monte Carlo result. Despite these effects, our analytic approximation to the perturbation cooling time remains in good agreement with the Monte Carlo (Figure 3-6), with the largest disagreement of 50% around optical depth unity, which arises primarily from inaccuracies in the mid-plane temperature.

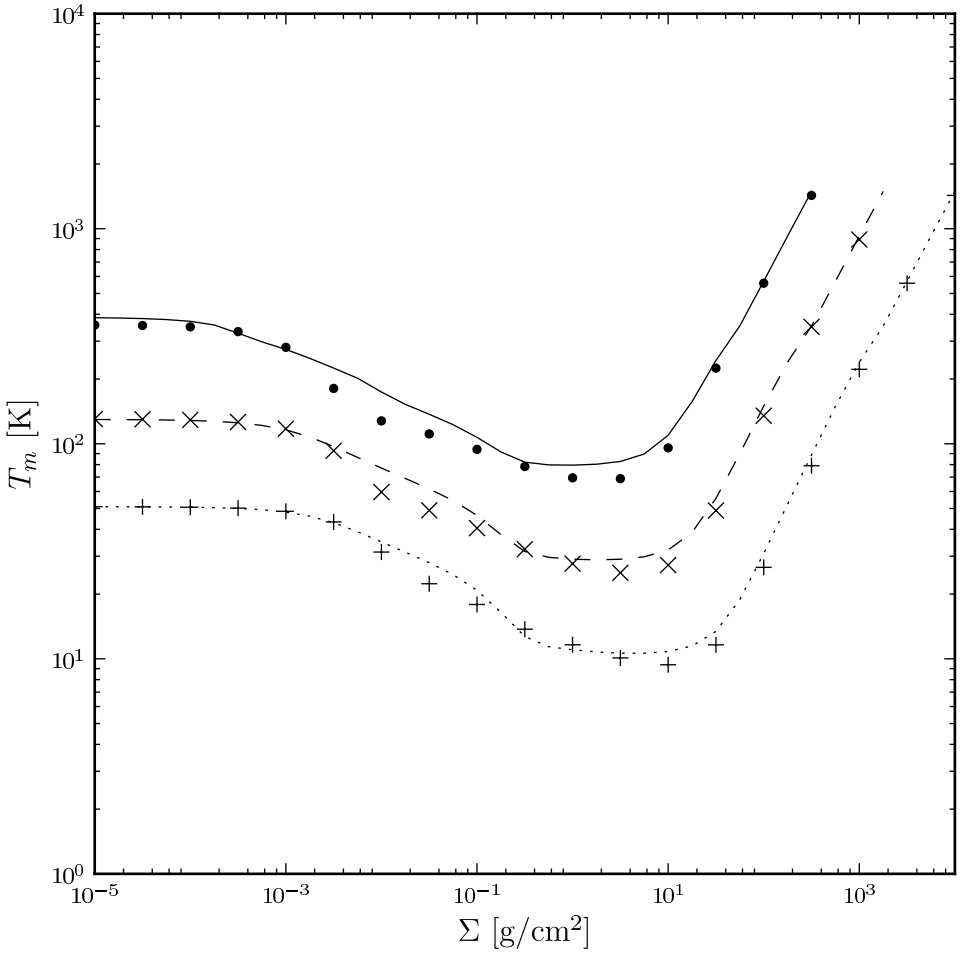

Figure 3-4: Same as Figure 3-1, but with the dust opacity of Wood et al. (2002).

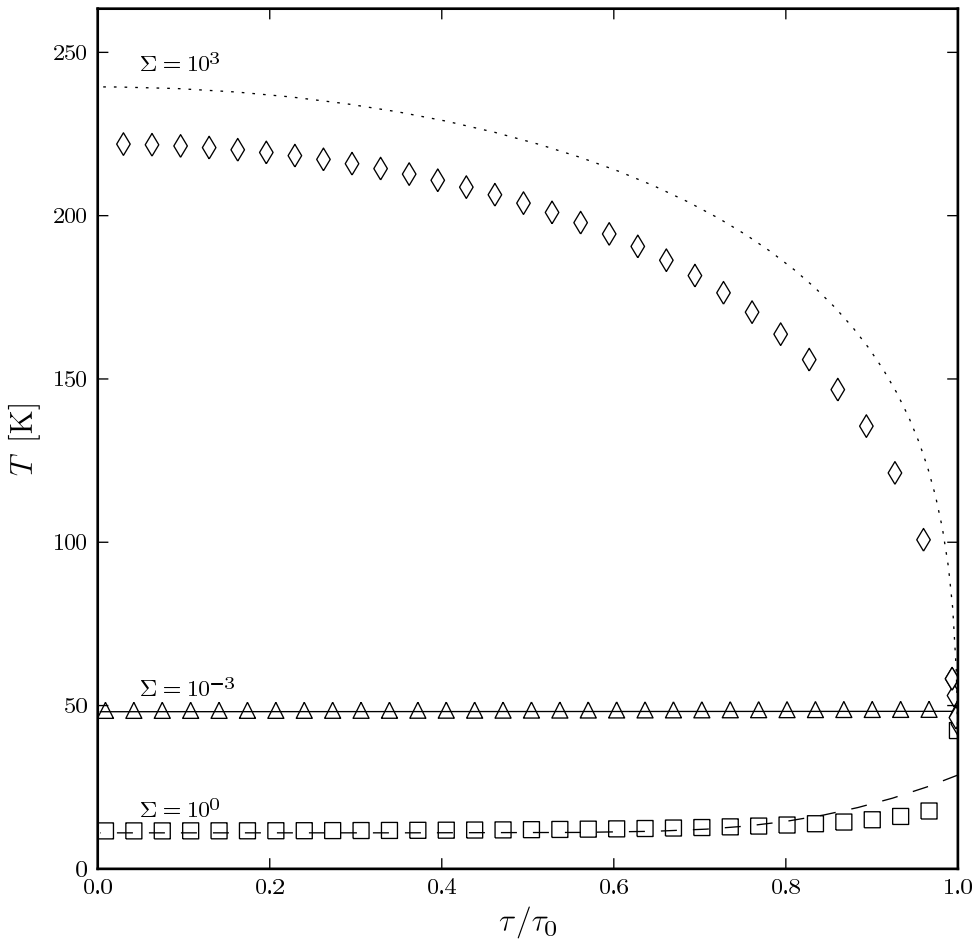

Figure 3-5: Same as Figure 3-2, but with the dust opacity of Wood et al. (2002).

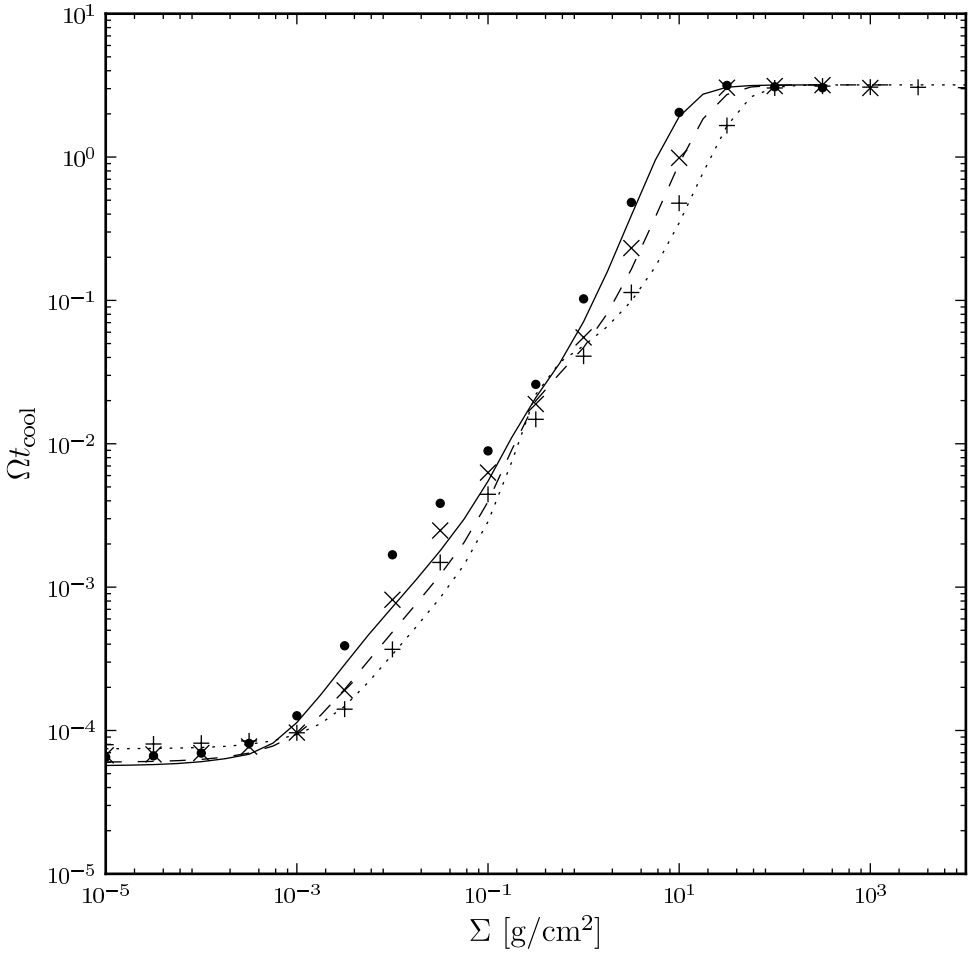

Figure 3-6: Same as Figure 3-3, but with the dust opacity of Wood et al. (2002).

Chapter 4

Fragment and Disk Masses

In this chapter, we consider the planet Fomalhaut b (Kalas et al., 2008), the triple-planet system HR 8799 (Marois et al., 2008), and the potential protoplanet orbiting HL Tau (Greaves et al., 2008). Each of these systems possesses at least one planet with orbital characteristics favored by the disk fragmentation mechanism. By determining the range of surface densities required to form a giant planet with the same semi-major axis as these observed planets, we can infer the range of disk masses needed for the fragmentation mechanism to have operated in these systems.

4.1 Fragment Masses

When determining if disk fragmentation is a viable mechanism for forming giant planets, an important point to consider is the issue of producing the proper planetary mass of a few $M_{\rm Jupiter}$. While a full treatment of this problem is beyond the scope of this work, we provide a toy model to argue that this is likely to be the case.

If $Q \lesssim 1$ at some radius r, the disk becomes gravitationally unstable. Supposing m spiral arms form, each arm has local surface density

$$\Sigma_{\rm arm} = \frac{\pi \cos\varphi}{m} \frac{r}{R} \Sigma \ , \tag{4.1}$$

where Σ is the original surface density of the previously axisymmetric disk, R is the current width of the spiral arms, and φ is the winding angle of a logarithmic spiral. For simplicity, we assume that most of the disk mass is confined to the spiral arms, while the space between the arms is effectively empty.

If $\Omega t_{\rm cool} \gtrsim 1$, then the spiral arms are pressure supported and are stable against fragmentation. However, if $\Omega t_{\rm cool} \lesssim 1$, then the arms are instead supported by centrifugal forces. As R continues to decrease, they will fragment radially once the centrifugal support is lost. Balancing self-gravity against the centrifugal support, $\Omega^2 R = \pi G \Sigma_{\rm arm}$, fragmentation occurs when

$$R < R_f = r^2 \sqrt{\frac{\pi^2 \cos\varphi}{m} \frac{\Sigma}{M_\star}} \ , \tag{4.2}$$

where $M_\star$ is the stellar mass. The fragment mass is $\pi R_f^2 \Sigma_{\rm arm}$, so assuming a few moderately wound spiral arms $\pi^2 \cos\varphi / m \sim 1$, we find a characteristic fragment mass

$$M_f \sim 1 M_{\rm Jupiter} \left(\frac{\Sigma}{10 \text{ g cm}^{-2}} \right)^{3/2} \left(\frac{M_\star}{M_\odot} \right)^{-1/2} \left(\frac{r}{100 \text{ AU}} \right)^3 \ , \tag{4.3}$$

which is consistent with our requirement to produce Jupiter-mass planets.

4.2 Disk Mass Limits

The condition that both the Toomre Q and the cooling time be sufficiently small can be used to place limits on what disk surface densities lead to fragmentation. To be gravitationally unstable, the Toomre Q condition requires that the surface density be larger than a minimum, $\Sigma_{\rm min}$, while the cooling condition imposes a maximum surface density, $\Sigma_{\rm max}$. Therefore, local disk fragmentation is only possible if $\Sigma_{\rm min} < \Sigma < \Sigma_{\rm max}$. It of course follows that for fragmentation to be possible at all, $\Sigma_{\rm min}$ must be less than $\Sigma_{\rm max}$. This limits the range of radii were fragmentation is even a possibility.

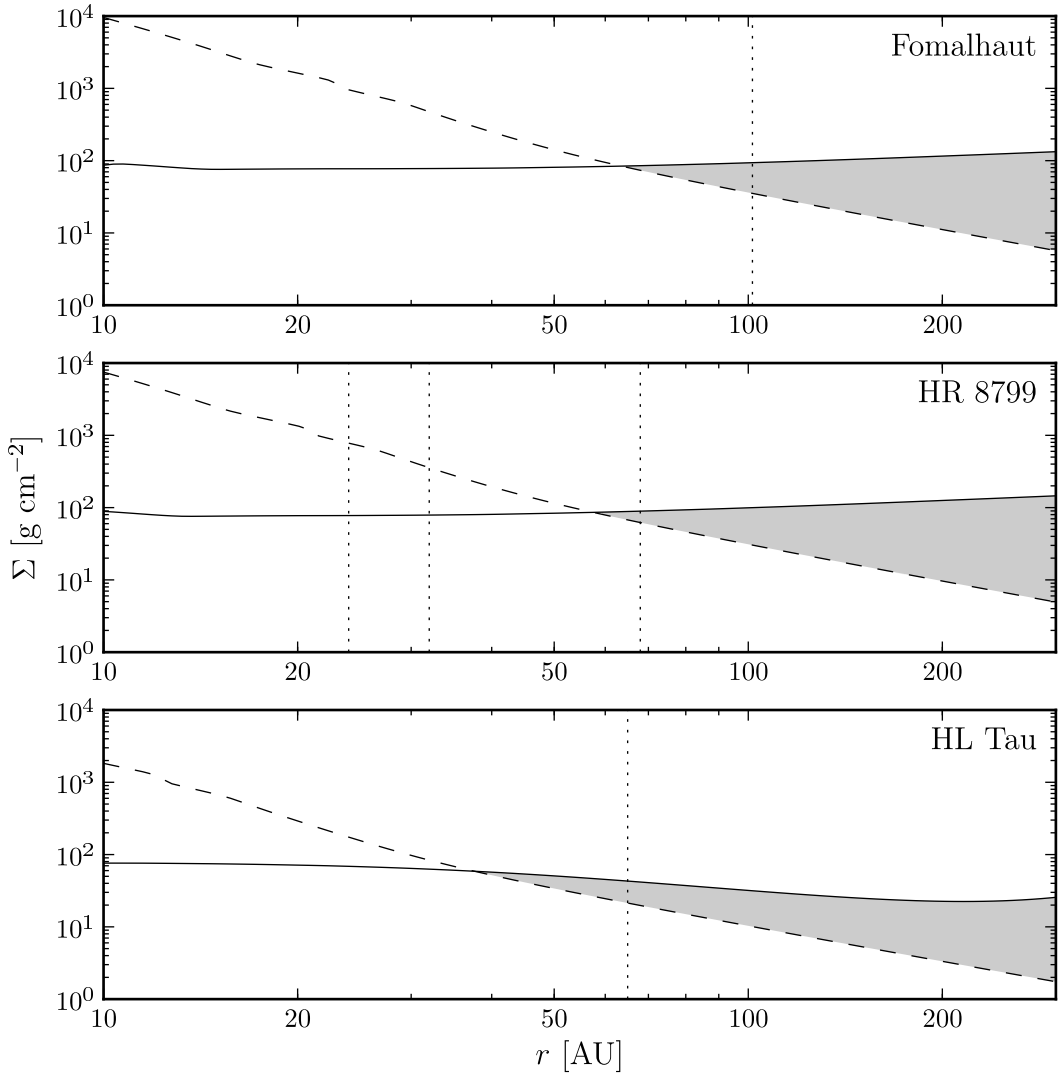

Figure 4-1: Surface density limits for disk fragmentation. The solid line denotes $\Sigma_{\rm max}$, which is the maximum surface density for the cooling time constraint. The dashed line denotes the minimum surface density for fragmentation, $\Sigma_{\rm min}$, which is the locus Toomre $Q = 1$. Disk fragmentation is only allowed in the region $\Sigma_{\rm max} > \Sigma_{\rm min}$, which is shaded gray. The locations of known planets are plotted as vertical dotted lines.

Table 4.1: Parameters Used for Each System

Object	$M_\star$ ($M_\odot$)	$R_\star$ ($R_\odot$)	$T_\star$ (K)	$r_{\rm planet(s)}$ (AU)
Fomalhaut b	2.0	1.8	8500	$>101.5^a$
HR 8799 b, c, d	1.5	1.8	8200	68, 38, 24^b
HL Tau b	0.3	0.6	3700	65^c

[a]Chiang et al. (2009)
[b]Marois et al. (2008)
[c]Greaves et al. (2008)

In Figure 4-1, we plot $\Sigma_{\rm min}$ and $\Sigma_{\rm max}$ for the systems Fomalhaut, HR 8799, and HL Tau, using the parameters listed in Table 4.1. In all cases we used an accretion rate of $10^{-6} M_\odot$/yr (which sets the net Eddington flux H_0), a mean molecular weight for the disk of $\mu = 2.33$, and an adiabatic gas constant of $\gamma = 1.43$. The temperature is determined from Equation (2.18), using a flared disk model with a power law scale height $h \propto r^{5/4}$, which determines the angle of incidence of the *external* radiation (Kenyon & Hartmann, 1987)

$$\mu_\star = \frac{dh/dr - h/r}{\sqrt{[1 + (h/r)^2][1 + (dh/dr)^2]}} \ . \tag{4.4}$$

We use the dust opacity of Cotera et al. (2001), which assumes icy dust grains. We note that the stellar parameters in Table 4.1 are not necessarily appropriate if planet formation occurs during the Class 0/I phase when the star is significantly more luminous. However, our results are relatively insensitive to this effect, since T_m is only weakly dependent on the stellar luminosity.

Each system presented here has a planet that might have formed via disk fragmentation, assuming that the local surface density had a value between $\Sigma_{\rm min}$ and $\Sigma_{\rm max}$ for at least a few orbital periods. By assuming a power law for the surface density, $\Sigma \propto r^{-p}$, we can calculate a range of disk masses (interior to $r_{\rm planet}$) that satisfies this

Table 4.2: Range of Disk Masses that Fragment

Object	Σ (g cm^{-2})	M_d ($p = 0.5$) ($M_\odot$)	M_d ($p = 1.0$) ($M_\odot$)	M_d ($p = 1.5$) ($M_\odot$)	M_f ($M_{\rm Jupiter}$)
Fomalhaut b	35–94	0.17–0.45	0.26–0.68	0.51–1.36	5–21
HR 8799 b	62–89	0.14–0.19	0.20–0.29	0.41–0.58	4–7
HL Tau b	21–43	0.04–0.09	0.06–0.13	0.13–0.26	2–4

condition.

A survey of 24 circumstellar disks by Andrews & Wiliams (2007) found $p \approx 0.0$–1.0 with an average of $p \approx 0.5$, while the hydrodynamical simulations of Vorobyov & Basu (2009) found $p \approx 1.0$–2.0 with an average around $p \approx 1.5$. Disk mass limits M_d for $p = 0.5$, 1.0 and 1.5, along with the more fundamental surface density limits are given in Table 4.2. We also provide the characteristic fragment mass (approximate planet mass) M_f from Equation (4.3) that we would expect from the disk fragmentation mechanism. Also note that, in order to be conservative, we are using the smallest radius found by Chiang et al. (2009) for Fomalhaut b. Using one of their better fits (e.g. 115 AU) will decrease our lower disk mass limit by a few percent, increase our upper disk mass limit by $\approx 30\%$ (which would make fragmentation slightly easier), and increase the characteristic fragment mass by $\approx 50\%$.

4.3 Discussion

While the ranges in Table 4.2 only span a factor of a few, this is not by itself a significant limitation. Even if the local surface density is above the upper instability limit, fragmentation may still occur since the surface density must eventually drop through the unstable regime as the disk evolves and dissipates. The caveat is that the surface density needs to evolve on a timescale longer than an orbital period so that there can be sufficient time to fragment.

Our minimum disk masses for Fomalhaut b, HR 8799 b, and HL Tau b are about

an order of magnitude larger than those inferred from observations (Andrews & Wiliams, 2007). Note, however, that this is a problem for all planet formation models in general. Even core accretion models require an enhanced surface density (although to a somewhat lesser extent) (Pollack et al., 1996; Inaba et al., 2003). One possible mechanism for increasing the surface density is mass loading from an infalling envelope (Vorobyov & Basu, 2006). Conversely, current estimates of disk masses may be too low because they depend on: 1) the extrapolation of surface densities in the outermost regions of the disk to the inner disk, and 2) the rather uncertain dust opacity. For example, larger dust grains would require larger disk masses to fit the observed spectral energy distributions (Andrews & Wiliams, 2007).

As further evidence for underestimated disk masses, numerical hydrodynamical simulations by Vorobyov (2009) found disk masses much higher than those of Andrews & Wiliams (2007). In particular, stars like Fomalhaut and HR 8799 can support disks as large as 0.5 $M_{\odot}$, while HL Tau could have a disk as massive as 0.1 $M_{\odot}$, all of which are within our limits for disk fragmentation. We caution, however, that our choice of opacity model can have a major effect on our results. For example, decreasing the dust opacity raises the temperature and decreases the cooling time in the outer disk, resulting in disk fragmentation at smaller radii. On the other hand, increasing the opacity would have the opposite effect.

Regardless of the above considerations, HR 8799 c and d are too close to their parent star to have formed *in situ* via fragmentation under the conditions modeled here. Appealing to chronically overestimated dust opacity can only get us so far. Dropping the opacity by an order of magnitude brings HR 8799 c into the fragmentation zone, but still leaves HR 8799 d out. Likewise, twiddling other parameters can also move the fragmentation radius inward, but reaching the required 24 AU with reasonable parameters does not seem possible. We therefore conclude that HR 8799 c and d likely did not form *in situ* as the result of disk fragmentation (of course, they could

have formed at larger radii were the disk is more likely to fragment and migrated inward).

For those planets that could form by disk fragmentation, we find characteristic fragment masses (approximate planet masses) of a few $M_{\rm Jupiter}$ for the lower end of unstable disk surface density. Our estimates are mostly consistent with expectations, although Chiang et al. (2009) found Fomalhaut b to have an upper mass limit of 3 $M_{\rm Jupiter}$, which is 60% lower than our lowest estimate of 5 $M_{\rm Jupiter}$. Nonetheless, considering the crudeness of Equation (4.3), this discrepancy does not rule out the possibility that Fomalhaut b formed as a result of disk fragmentation.

Chapter 5

Enhancements to Cooling

5.1 Vertically Displaced Perturbation

We now consider the case where the temperature perturbation is no longer at the disk mid-plane. By moving the perturbation closer to the surface, we provide a shorter path for radiation to escape. This will consequently decrease the cooling time. If this situation arises due to an inclined orbit, then the height of the perturbation is the "cooling-averaged" height, which would be heavily weighted to the maximum height where the cooling is most efficient.

Since the details of the perturbation have no effect on the background solution, the effects of moving the perturbation away form the mid-plane must be fully contained within the perturbed Planck function (eq. [2.19]). We start by re-writing Equation (2.19) in the more general form

$$\Delta B = \frac{1}{f^{\rm diff}} \int_{\tau}^{\tau_0} \Delta H \, d\tau + \frac{\Delta H_+}{g^{\rm diff}} + \frac{\chi^{\rm diff}}{\kappa^{\rm diff}} \frac{d\Delta H}{d\tau} \ , \tag{5.1}$$

where

$$\Delta H = \begin{cases} -\Delta H_- & (\tau < \tau') \\ \Delta H_+ & (\tau > \tau') \end{cases}$$

with $\Delta H_+ = \Delta H(\tau_0)$, $\Delta H_- = \Delta H(-\tau_0)$, and τ' the optical depth coordinate of the perturbation. The cooling time (eq. [2.5]) takes the form

$$t_{\rm cool} = \frac{1}{16}\frac{c_{\rm m}^2}{\gamma - 1}\frac{1}{\sigma T_{\rm m}^4}\frac{1}{\chi}\int_{-\tau_0}^{\tau_0}\left(\frac{B}{B_m}\right)^{-3/4}\frac{\Delta B}{\Delta H_+ + \Delta H_-}\,{\rm d}\tau \ . \tag{5.2}$$

Note that for nonzero τ', $\Delta H_+ \neq \Delta H_-$. To find the relationship between $\Delta H_+$and ΔH_-, we use the fact that $\Delta B(\tau_0) = \Delta H_+/g^{\rm diff}$ and correspondingly, $\Delta B(-\tau_0) = \Delta H_-/g^{\rm diff}$ ($g^{\rm diff}$is the same on the top and bottom surfaces, since it is unperturbed). Thus

$$\Delta H_- = \Delta H_+ \frac{f^{\rm diff} + g^{\rm diff}(\tau_0 - \tau')}{f^{\rm diff} + g^{\rm diff}(\tau_0 + \tau')} \ , \tag{5.3}$$

and

$$\Delta B = (\Delta H_+ + \Delta H_-)\frac{\chi^{\rm diff}}{\kappa^{\rm diff}}\delta(\tau - \tau') + \begin{cases} \Delta H_-\left(\frac{\tau_0+\tau}{f^{\rm diff}} + \frac{1}{g^{\rm diff}}\right) & (\tau < \tau') \\ \Delta H_+\left(\frac{\tau_0-\tau}{f^{\rm diff}} + \frac{1}{g^{\rm diff}}\right) & (\tau > \tau') \ . \end{cases} \tag{5.4}$$

In the limit of a vertically isothermal disk ($B/B_m \to 1$), the cooling time (eq. [5.2]) can be integrated analytically, yielding

$$t_{\rm cool} = \frac{1}{16}\frac{c_{\rm m}^2}{\gamma - 1}\frac{1}{\sigma T_{\rm m}^4}\left[\frac{\chi^{\rm diff}\Sigma^2}{8 f^{\rm diff}}\left(1 - \frac{\tau'}{\tau_0}\right) + \frac{\Sigma}{2 g^{\rm diff}} + \frac{1}{\kappa^{\rm diff}}\right] \ . \tag{5.5}$$

We find that the effect of moving the perturbation away from the disk mid-plane is to decrease the optically thick contribution to the cooling time, while the optically thin and surface terms remain unaffected. One somewhat surprising consequence of this result is that a perturbation placed on the surface ($\tau' \to \pm\tau_0$) does not cool

infinitely quickly, or even at the optically thin limit (unless of course the disk is optically thin). Physically, a surface perturbation still heats the interior of the disk, but the bulk of the extra internal energy is stored much closer to the surface (in optical depth space) than in the case where the perturbation was on the mid-plane. Thus, it is the surface term that dominates for moderate to large optical depths.

The results of moving the perturbation to 0.5, 1, and 2 scale heights is shown in Figure 5-1. The limiting case of moving the perturbation all the way to the disk surface ($\tau' \rightarrow \pm\tau_0$) is also shown. We use the same stellar and disk parameters as in Section 3. Note that while a surface perturbation has the effect of reducing the perturbation cooling time below the critical fragmentation value of $\Omega t_{\rm cool} = 1$ everywhere (and for any $\alpha \gtrsim 10^{-4}$), the effects at one scale height are more subdued. Furthermore, the majority of the disk mass is—by definition—within a scale height of the mid-plane, reducing the likelihood that a disk would begin its fragmentation outside of that range. Therefore, a vertically displaced perturbation will probably only reduce the perturbation cooling time by a factor of a few at the most.

5.2 Dust Settling

Another effect that can decrease the cooling time is dust settling. For temperatures below dust sublimation ($\sim$ 1500 K), dust is by far the primary opacity source. On the other hand, since the gas-to-dust ratio is $\sim$ 100, most of the disk's mass (and thus internal energy) is stored in the gas. Consequently, if the dust has a smaller scale height than the gas (i.e., the dust has settled), then more of the internal energy is stored in the optically thin surface layers of the disk. In effect this changes the mapping between the spatial coordinates and the optical depth coordinates of the internal energy distribution.

To account for the effects of dust settling, we divide the disk into three layers:

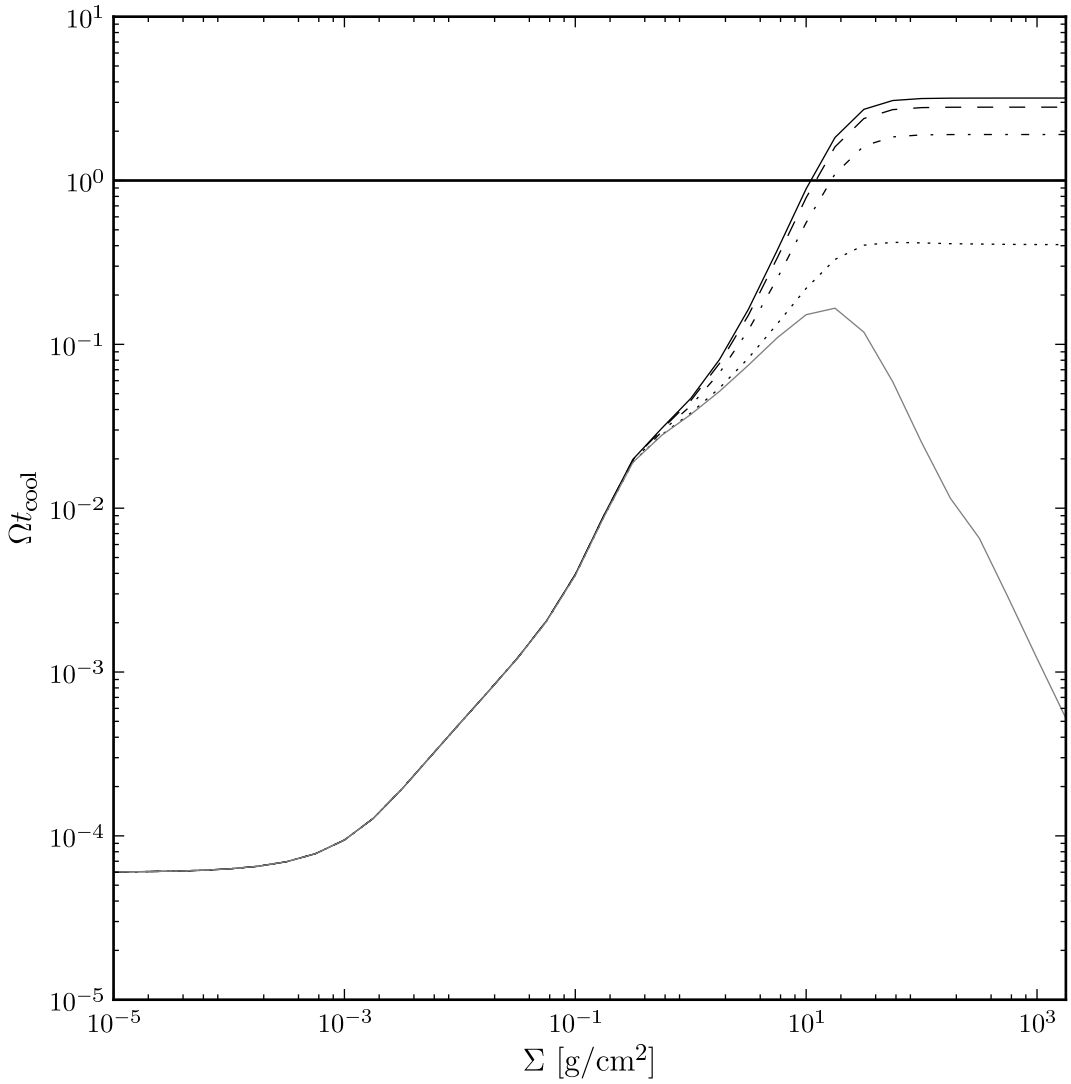

Figure 5-1: The cooling time as a function of surface density for a perturbation located at the mid-plane (solid black line), at half of a scale height (dashed line), at one scale height (dot-dashed line), at two scale heights (dotted line), and for the extreme case of a surface perturbation (gray solid line). The critical cooling time for fragmentation $\Omega t_{\rm cool} = 1$ is indicated by the bold, horizontal line. Comparisons are made at 10 AU from a 0.5 $M_\odot$, 2.0 $R_\odot$, 4000 K star, using the dust opacity of Wood et al. (2002) and $\alpha = 0.1$.

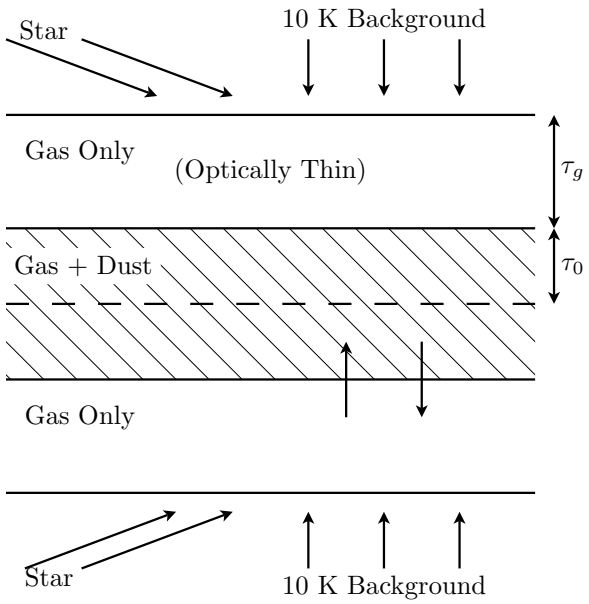

Figure 5-2: Sketch of our three-layer disk model, including the effects of external illumination from both the star and 10 K background, internal energy generation, and dust settling.

a layer of dust and gas centered about the disk mid-plane (which we call the *dust layer*), and two layers of optically thin gas surrounding it on either side (which we call *gas layers*). A sketch of our model is shown in Figure 5-2. For simplicity, we assume that the disk is in hydrostatic equilibrium, and that the gas has a Gaussian density distribution. Near the mid-plane (i.e., within the dust layer), the gas density will be slowly-varying, and thus we will assume it is constant. Furthermore, we will assume that the dust density is also constant within the dust layer, and that all of the dust has settled into this layer. The gas layer has surface density $\Sigma^{\rm gas}$ and optical depth $\tau_g = \chi^{\rm gas}\Sigma^{\rm gas}$. The dust layer has surface density $\Sigma^{\rm dust} = \Sigma_g^{\rm dust} + \Sigma_d^{\rm dust}$ and total optical depth $2\tau_0 = \chi^{\rm diff}\Sigma - 2\chi^{\rm gas}\Sigma^{\rm gas}$, where $\Sigma_g^{\rm dust}$ is the surface density of the gas within the dust layer, and $\Sigma_d^{\rm dust}$ is the surface density of the dust.

Given a gas-to-dust ratio $\varrho = \rho_g/\rho_d$ and dust settling h_d/h_g, the total surface

density Σ is divided according to

$$\frac{\Sigma_d^{\rm dust}}{\Sigma} = \frac{1}{\varrho+1} , \tag{5.6}$$

$$\frac{\Sigma_g^{\rm dust}}{\Sigma} = \frac{\varrho}{\varrho+1}\frac{h_d}{h_g} , \tag{5.7}$$

$$\frac{\Sigma^{\rm gas}}{\Sigma} = \frac{\varrho}{\varrho+1}\left(1-\frac{h_d}{h_g}\right) . \tag{5.8}$$

In addition, the internal energy generation is also split among the layers. Within the dust layer, the fractional internal energy generation

$$\begin{aligned}\frac{H_0}{H_{\rm tot}} &= \frac{\Sigma^{\rm dust}}{\Sigma} \\ &= \frac{\varrho}{\varrho+1}\left(\frac{1}{\varrho}+\frac{h_d}{h_g}\right) ,\end{aligned} \tag{5.9}$$

while in the gas layer

$$\begin{aligned}\frac{H_g}{H_{\rm tot}} &= \frac{\Sigma^{\rm gas}}{\Sigma} \\ &= \frac{\varrho}{\varrho+1}\left(1-\frac{h_d}{h_g}\right) ,\end{aligned} \tag{5.10}$$

where

$$H_{\rm tot} = \frac{9}{32\pi}\alpha c_m^2 \Omega\Sigma , \tag{5.11}$$

is the total energy generated by viscous heating (as in eq. [2.26]).

5.2.1 Dust Layer

In addition to just stellar illumination, the *external* radiation field (i.e., radiation impingent on the dust layer) now needs to include the effects of radiation from the gas layers. In addition, we use this opportunity to add in the effects of a background radiation field (i.e., a 10 K black body corresponding to the interior of a giant molec-

ular cloud). This background radiation field plays the role of setting a minimum temperature within the disk when both stellar illumination and viscous energy generation are weak. Studying the effects of a background radiation field is also interesting, because it allows for the potential inclusion of more exotic effects (e.g., a nearby OB association).

To account for these new sources of radiation, we split the *external* radiation into three components: *star* which corresponds to stellar irradiation, *surface* (or *surf)* which corresponds to radiation from the gas layers, and *background* (or *bg*) which corresponds to the 10 K background. The solutions to these radiation fields are identical to the *external* field found in Equations (2.14) and (2.15), with the exception that $\kappa^{\rm ext} \rightarrow \kappa^{\rm star}$, $\kappa^{\rm surf}$, or $\kappa^{\rm bg}$ (referring to the opacity of each respective radiation field within the dust layer). In addition, each new field has unique solutions to the boundary conditions $f^{\rm star}$, $f^{\rm surf}$, $f^{\rm bg}$, $H_0^{\rm star}$, $H_0^{\rm surf}$, and $H_0^{\rm bg}$. Thus,

$$H^{\rm star} = H_0^{\rm star} \frac{\sinh \beta^{\rm star} \tau}{\sinh \beta^{\rm star} \tau_0} \ , \tag{5.12}$$

$$H^{\rm surf} = H_0^{\rm surf} \frac{\sinh \beta^{\rm surf} \tau}{\sinh \beta^{\rm surf} \tau_0} \ , \tag{5.13}$$

$$H^{\rm bg} = H_0^{\rm bg} \frac{\sinh \beta^{\rm bg} \tau}{\sinh \beta^{\rm bg} \tau_0} \ , \tag{5.14}$$

and

$$J^{\rm star} = -\frac{\beta^{\rm star} \chi^{\rm diff}}{\kappa^{\rm star}} H_0^{\rm star} \frac{\cosh \beta^{\rm star} \tau}{\sinh \beta^{\rm star} \tau_0} \ , \tag{5.15}$$

$$J^{\rm surf} = -\frac{\beta^{\rm surf} \chi^{\rm diff}}{\kappa^{\rm surf}} H_0^{\rm surf} \frac{\cosh \beta^{\rm surf} \tau}{\sinh \beta^{\rm surf} \tau_0} \ , \tag{5.16}$$

$$J^{\rm bg} = -\frac{\beta^{\rm bg} \chi^{\rm diff}}{\kappa^{\rm bg}} H_0^{\rm bg} \frac{\cosh \beta^{\rm bg} \tau}{\sinh \beta^{\rm bg} \tau_0} \ , \tag{5.17}$$

where

$$\beta^{\rm star} = \frac{\chi^{\rm star}}{\chi^{\rm diff}}\sqrt{\frac{\kappa^{\rm star}}{\chi^{\rm star}}\frac{1}{f^{\rm star}}}\ , \tag{5.18}$$

$$\beta^{\rm surf} = \frac{\chi^{\rm surf}}{\chi^{\rm diff}}\sqrt{\frac{\kappa^{\rm surf}}{\chi^{\rm surf}}\frac{1}{f^{\rm surf}}}\ , \tag{5.19}$$

$$\beta^{\rm bg} = \frac{\chi^{\rm bg}}{\chi^{\rm diff}}\sqrt{\frac{\kappa^{\rm bg}}{\chi^{\rm bg}}\frac{1}{f^{\rm bg}}}\ . \tag{5.20}$$

The solutions to the expanded set of boundary conditions is given in Appendix A.

The *diffuse* radiation field is also similar to the single layer model, with the exception that it now includes three terms instead of one for the *external* radiation. The *diffuse* mean intensity (eq. [2.17]) becomes

$$\begin{aligned} J^{\rm diff} = {} & H_0\left(\frac{\tau_0^2-\tau^2}{2f^{\rm diff}\tau_0}+\frac{1}{g^{\rm diff}}\right)+\Delta H_0\left(\frac{\tau_0-|\tau|}{f^{\rm diff}}+\frac{1}{g^{\rm diff}}\right) \\ & -H_0^{\rm star}\left(\frac{\cosh\beta^{\rm star}\tau_0-\cosh\beta^{\rm star}\tau}{\beta^{\rm star}f^{\rm diff}\sinh\beta^{\rm star}\tau_0}+\frac{1}{g^{\rm diff}}\right) \\ & -H_0^{\rm surf}\left(\frac{\cosh\beta^{\rm surf}\tau_0-\cosh\beta^{\rm surf}\tau}{\beta^{\rm surf}f^{\rm diff}\sinh\beta^{\rm surf}\tau_0}+\frac{1}{g^{\rm diff}}\right) \\ & -H_0^{\rm bg}\left(\frac{\cosh\beta^{\rm bg}\tau_0-\cosh\beta^{\rm bg}\tau}{\beta^{\rm bg}f^{\rm diff}\sinh\beta^{\rm bg}\tau_0}+\frac{1}{g^{\rm diff}}\right)\ , \end{aligned} \tag{5.21}$$

and the Planck function in the dust layer becomes

$$B^{\rm dust} = J^{\rm diff}+\frac{\chi^{\rm diff}}{\kappa^{\rm diff}}\frac{H_0}{\tau_0}+\frac{\kappa^{\rm star}}{\kappa^{\rm diff}}J^{\rm star}+\frac{\kappa^{\rm surf}}{\kappa^{\rm diff}}J^{\rm surf}+\frac{\kappa^{\rm bg}}{\kappa^{\rm diff}}J^{\rm bg}+2\frac{\chi^{\rm diff}}{\kappa^{\rm diff}}\Delta H_0\delta(\tau)\ . \tag{5.22}$$

The perturbed Planck function in the dust layer remains unchanged from Equation (2.19) (or eq. [5.4] for a vertically displaced perturbation).

5.2.2 Gas Layer

Since the gas layer is optically thin, the mean intensity is set by the impingent radiation from the star, the 10 K background, and the dust layer, plus local internal energy generation (we assume that the contribution from reprocessed radiation is negligible). For simplicity, we assume that the gas layer has gray opacity. It follows that the mean intensity for the gas layer

$$\begin{aligned} J^{\rm gas} &= \frac{H_\star}{2\mu_\star}\left[1+\exp\left(-\frac{2\tau_0+\tau_g}{\mu_\star}\right)\right]+\frac{\sigma T_{\rm bg}^4}{2\pi}\left[1+E_2(2\tau_0+\tau_g)\right] \\ &\quad +\frac{H_0-H_0^{\rm star}-H_0^{\rm surf}-H_0^{\rm bg}}{g^{\rm diff}}+\frac{\Delta H_0}{g^{\rm diff}}\ , \end{aligned} \tag{5.23}$$

where E_2 is an exponential integral and $T_{\rm bg} = 10$ K is the temperature of the background radiation field. Assuming radiative equilibrium, the Planck function in the gas layer

$$B^{\rm gas} = J^{\rm gas} + \frac{\chi^{\rm gas}}{\kappa^{\rm gas}}\frac{H_g}{\tau_g}\ . \tag{5.24}$$

Note that the perturbed Planck function

$$\Delta B^{\rm gas} = \frac{\Delta H_0}{g^{\rm diff}} = \Delta B^{\rm dust}(\tau_0)\ , \tag{5.25}$$

is set by $\Delta B^{\rm dust}$ at the top of the dust layer, regardless of whether the perturbation is located at the disk mid-plane, or is displaced as in § 5.1.

5.2.3 Cooling Time With Dust Settling

There are three contributions to the excess internal energy, and thus the cooling time: 1) gas in the dust layer, 2) dust in the dust layer, and 3) gas in the two gas layers. In addition, each of these contributions is weighted by the specific heat of

their constituents. The cooling time (eq. [2.3]) becomes

$$t_{\rm cool} = \frac{1}{4\pi(\Delta H_+ + \Delta H_-)} \frac{k_B}{m_H} \left[\frac{1}{\mu_g(\gamma_g - 1)} \int_{-z_0}^{z_0} \Delta T^{\rm dust} \rho_g^{\rm dust} dz + \frac{1}{\mu_d(\gamma_d - 1)} \int_{-z_0}^{z_0} \Delta T^{\rm dust} \rho_d^{\rm dust} dz + \frac{1}{\mu_g(\gamma_g - 1)} \int_{z_0}^{\infty} \Delta T^{\rm gas} \rho_g^{\rm gas} dz \right] , \quad (5.26)$$

where μ_g, γ_g, and ρ_g are the mean molecular weight, adiabatic gas constant, and density for the gaseous component of the disk. The same quantities with a d subscript correspond to the dust component of the disk. Similarly, the *dust* and *gas* superscripts refer to the corresponding layer. The z-coordinate of the top/bottom of the dust layer is $\pm z_0$.

Since the dust component is the dominant opacity source, we make the simplification that $\Sigma\chi^{\rm diff} = \Sigma_d \chi_d$, where χ_d is the opacity of the dust component. Thus, in the dust layer, $d\tau = \chi_d \rho_d dz = (\Sigma/\Sigma_d)\chi^{\rm diff}\rho_d dz$. Since $\rho_g/\rho_d = \Sigma_g h_d / \Sigma_d h_g$, and using Equation (2.4) to express ΔT in terms of ΔB,

$$t_{\rm cool} = \frac{1}{16} \frac{c_m^2}{\gamma - 1} \frac{1}{\sigma T_m^4} \left[\frac{1}{\chi^{\rm diff}} \left(\frac{\Sigma_g}{\Sigma} \frac{h_d}{h_g} + \frac{\Sigma_d}{\Sigma} \phi_d \right) \int_{-\tau_0}^{\tau_0} \left(\frac{B^{\rm dust}}{B_m} \right)^{-3/4} \frac{\Delta B^{\rm dust}}{\Delta H_+ + \Delta H_-} d\tau + \frac{\Sigma^{\rm gas}}{g^{\rm diff}} \left(\frac{B^{\rm gas}}{B_m} \right)^{-3/4} \right] , \quad (5.27)$$

where we have allowed for a vertically displaced perturbation (recall $H_+ = H_- = H_0$ if the perturbation is at the mid-plane). In addition, we have assumed that the gas component dominates the internal energy of the disk, and thus $\gamma_g \approx \gamma$ and $\mu_g \approx \mu$. The factor

$$\phi_d = \frac{\mu(\gamma - 1)}{\mu_d(\gamma_d - 1)} , \quad (5.28)$$

is the relative contribution of the dust to the specific heat of the disk. Note that while the contribution of the dust to the internal energy is in general trivial, in the

limit of extreme dust settling ($h_d/h_g \to 0$) this term can become dominant.

If we assume that the dust grains follow the Debye model, then

$$\frac{1}{\gamma_d - 1} = \begin{cases} \frac{12\pi^4}{5}\left(\frac{T_m}{T_D}\right)^3 & (T_m \ll T_D) \\ 3 & (T_m \gg T_D)\ , \end{cases} \tag{5.29}$$

where $T_D \approx 700$ K (for interstellar dust grains) is the Debye temperature (Andriesse, 1977). For a gas-to-dust ratio $\varrho = 100$, and assuming $\mu(\gamma - 1) \sim 1$ and $\mu_d \sim 30$; $\phi_d \sim 10(T_m/T_D)^3$ in the low-temperature limit, while $\phi_d \sim 0.1$ in the high-temperature limit.

We now evaluate Equation 5.27 for different degrees of dust settling. We use $\chi^{\rm gas} = \kappa^{\rm gas} = 10^{-4}$ to ensure that the gas layer remains optically thin over the range of surface densities considered. While this is probably an underestimate, we note that the perturbation cooling time is only weakly dependent on the value of the gas opacity, so long as the gas layer has a much lower optical depth than the dust layer. In addition, we use the scale height of the dust layer to determine $\mu_\star$, noting that this leads to an increasingly shallow angle of incidence as dust settling progresses. We assume that the disk flaring continues to follow $h_d \propto r^{5/4}$, independent of the degree of dust settling

The effects of dust settling are illustrated in Figure 5-3. Shown are the perturbation cooling times when $h_d/h_g = 1$ (unsettled), 0.5, 0.1, 0.01, and 0 (completely settled). Note that when $h_d/h_g \lesssim 0.1$, the disk is below the critical cooling time for a greatly increased range of surface densities (assuming $\xi\alpha \approx 0.1$).

As dust settling proceeds below $h_d/h_g \approx 0.1$, the perturbation cooling time actually begins to increase for the largest surface densities. This behavior is due to the increasing amount of excess internal energy that is stored within the gas layers. Since the optically thin gas layer is isothermal, the perturbation cooling time is longer

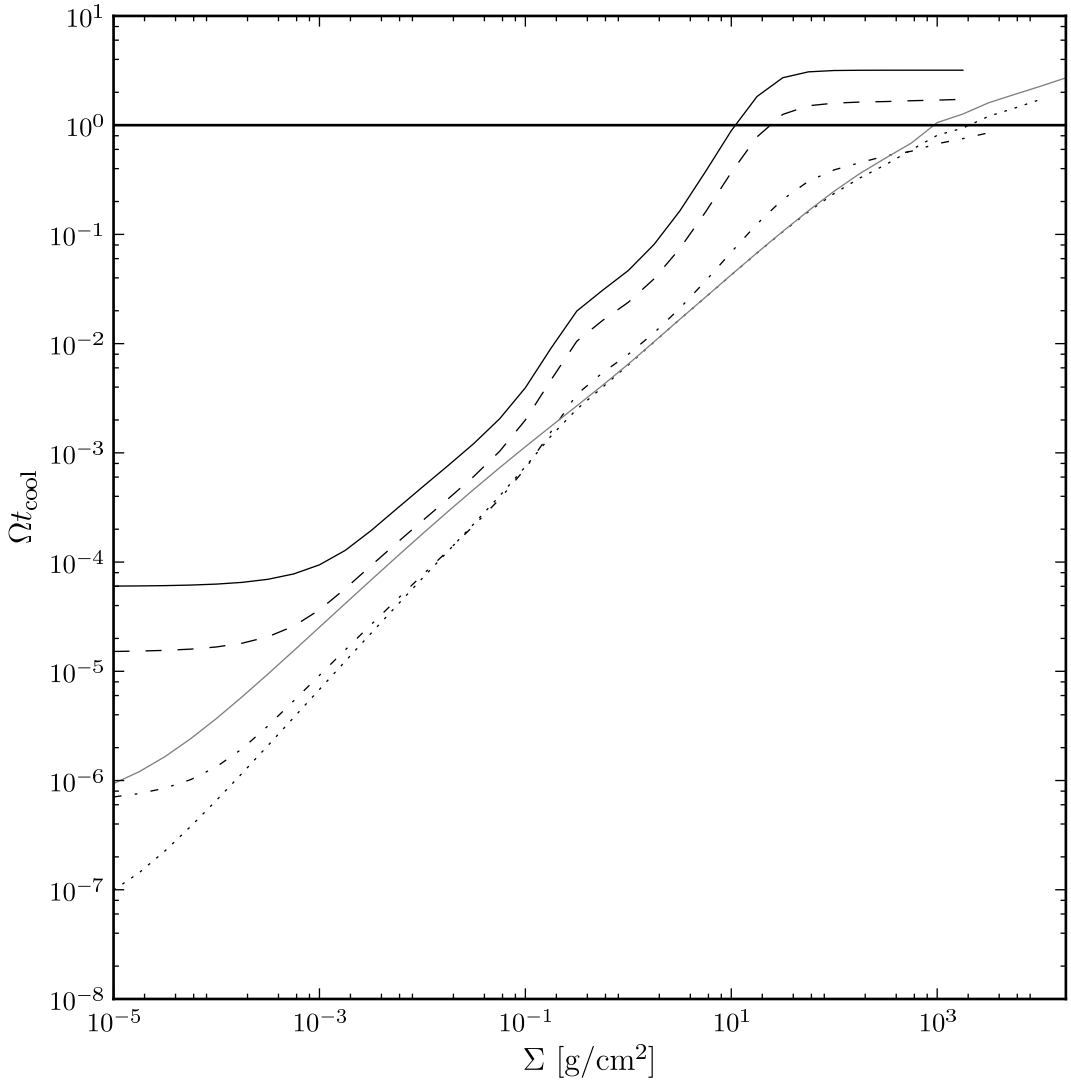

Figure 5-3: The perturbation cooling time as a function of surface density for a disk with no dust settling $h_d/h_g = 1$ (solid black line), for $h_d/h_g = 0.5$ (dashed line), for $h_d/h_g = 0.1$ (dot-dashed line), for $h_d/h_g = 0.01$ (dotted line), and for the extreme case $h_d/h_g = 0$ (gray solid line). The critical cooling time for fragmentation $\Omega t_{\rm cool} = 1$ is indicated by the bold, horizontal line. Comparisons are made at 10 AU from a 0.5 $M_\odot$, 2.0 $R_\odot$, 4000 K star, using the dust opacity of Wood et al. (2002) and $\alpha = 0.1$.

than it would be if there were a temperature gradient (as there is in the dust layer). Note that if Σ is allowed to increase to high enough values, the disk will eventually return to the opacity-independent, self-heated limit (eq. [2.29]), although since this only occurs after dust sublimation begins, we do not consider this limit further. A comparison of the effects of dust settling on maximum surface density for fragmentation $\Sigma_{\rm max}$ (the locus $\Omega t_{\rm cool} = 1$) at 1, 10, and 100 AU is shown in Figure 5-4. Note that $\Sigma_{\rm max}$ is maximized when $h_d/h_g \sim 0.1$, but any significant degree of dust settling ($h_d/h_g \lesssim 0.3$) serves to significantly increase $\Sigma_{\rm max}$ compared to the unsettled case.

Of additional interest is the case where the disk is both settled and harbors a perturbation offset from the mid-plane. By changing the mapping between the dust and gas scale heights, a perturbation located at one gas scale height can simultaneously be at many dust scale heights, and thus behave as if it were at the surface. An example of this case is examined in Figure 5-5, where the perturbation is at one gas scale height, and $h_d/h_g = 0.5$, 0.1, and 0.01. Unsurprisingly, even modest dust settling is sufficient to keep $\Omega t_{\rm cool} < 1$ for all $\Sigma \lesssim 10^3$.

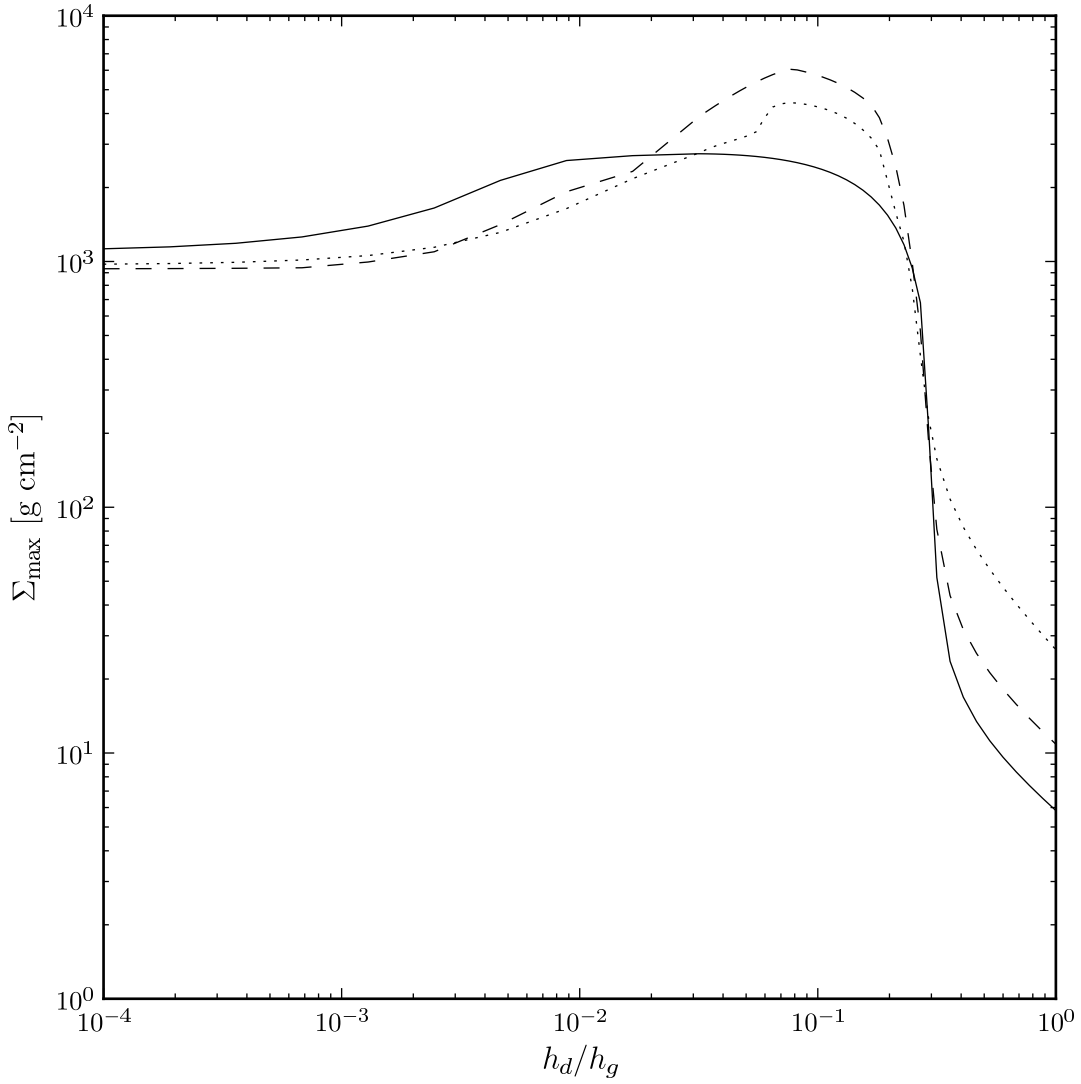

Figure 5-4: The maximum surface density for fragmentation, $\Sigma_{\rm max}$, as a function of the dust settling h_d/h_g for a 0.5 $M_\odot$, 2.0 $R_\odot$, 4000 K star at 1, 10, and 100 AU (solid, dashed, and dotted lines, respectively).

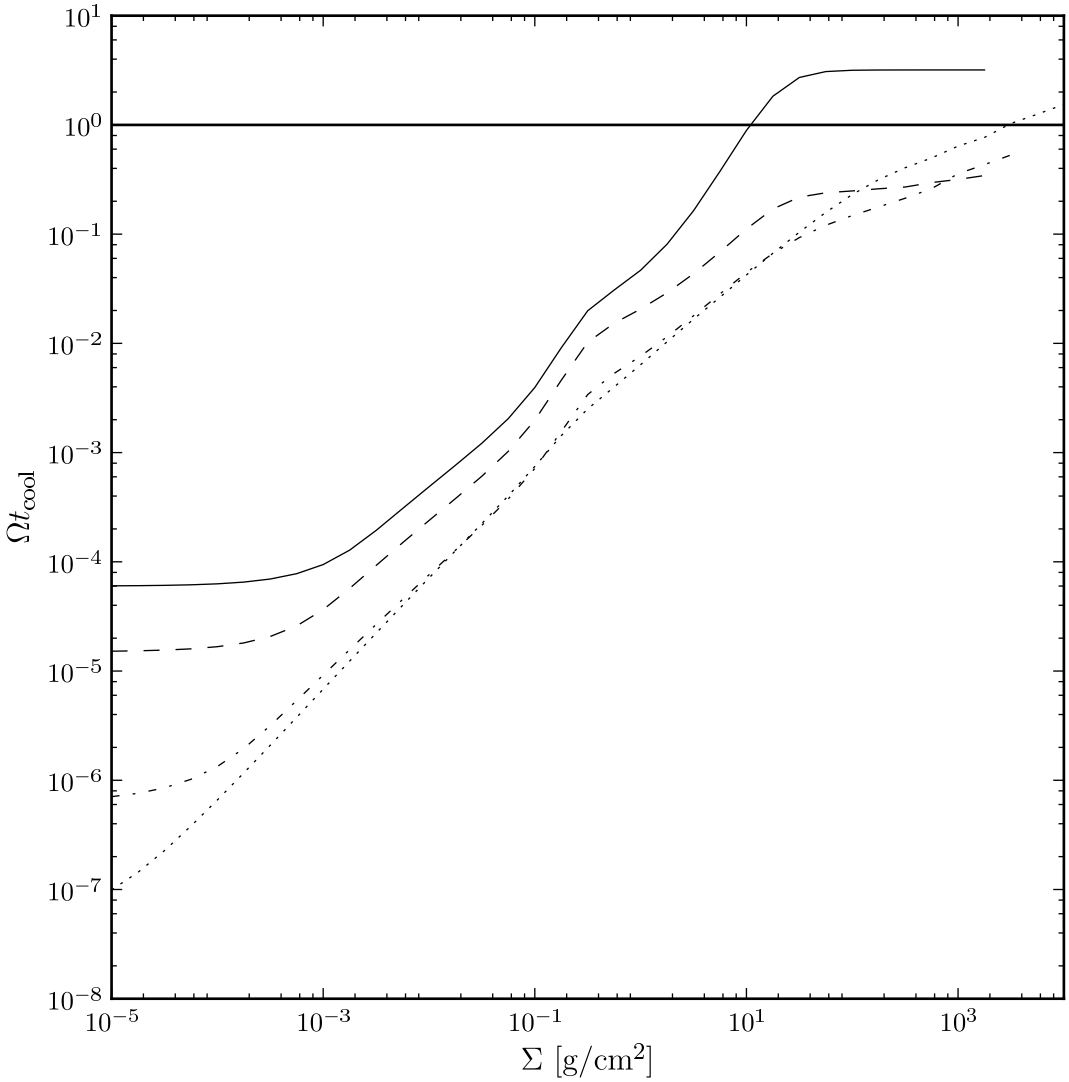

Figure 5-5: The cooling time as a function of surface density for a perturbation located at one gas scale height and with dust settling. Comparisons are made for $h_d/h_g = 0.5$ (dashed line), for $h_d/h_g = 0.1$ (dot-dashed line), and for $h_d/h_g = 0.01$ (dotted line). The unmodified perturbation cooling time is given by the black solid line for comparison. The critical cooling time for fragmentation $\Omega t_{\rm cool} = 1$ is indicated by the bold, horizontal line. Comparisons are made at 10 AU from a 0.5 $M_\odot$, 2.0 $R_\odot$, 4000 K star, using the dust opacity of Wood et al. (2002) and $\alpha = 0.1$.

Chapter 6

Consequences of Dust Settling

In this chapter, we use our technique for calculating perturbation cooling times to explore a range of stellar and disk parameters to determine which systems are the best candidates to form giant planets via disk fragmentation. We use the three-layer model described in § 5.2 with viscosity parameter $\alpha = 0.1$, $\chi^{\rm gas} = \kappa^{\rm gas} = 10^{-4}$ cm g^{-2}, and with the dust opacities of Wood et al. (2002). Since disks are most massive during the pre-main sequence phase (Vorobyov, 2009), we use the evolutionary tracks of Siess et al. (2000) to find the appropriate luminosity as a function of age for low- to intermediate-mass stars.

6.1 Instability Limits

In Figures 6-1–6-3, we plot $\Sigma_{\rm max}$ and $\Sigma_{\rm min}$ following the approach of § 4.2 for 0.1, 0.2, 0.5, 1, 2, and 5 $M_\odot$ at ages of 0.5, 1, 5, and 10 Myr. Figure 6-1 shows the case with no dust settling (i.e., $h_d/h_g = 1$), Figure 6-2 shows a case with partial dust settling ($h_d/h_g = 0.5$), and Figure 6-3 shows a case with significant dust settling ($h_d/h_g = 0.1$). Since the perturbation cooling time depends on the stellar luminosity, $\Sigma_{\rm max}$ is a function of age. However, the effect on the minimum fragmentation radius is only of order 10%, indicating that the stellar age has little effect on the instability

criteria (however the increased disk mass when the system is still young remains important). In addition, when dust settling is significant, the age-dependence of the perturbation cooling time vanishes, since the shallow angle of incidence for the stellar radiation causes it to be completely absorbed within the gas layers. Furthermore, a dust-settled disk will be well into the self-heated limit at $\Sigma_{\rm max}$, further reducing the effect of the stellar illumination.

The most striking consequence of dust settling is the greatly increased range of disk radii and surface densities where fragmentation is allowed. The maximum surface density for fragmentation $\Sigma_{\rm max}$ is enhanced by several orders of magnitude when the dust has settled to a tenth of the gas scale height ($h_d/h_g = 0.1$) compared to the unsettled case. More importantly, the minimum fragmentation radius moves approximately an order of magnitude closer to the star. This consequence is further explored in Figures 6-4–6-6.

We plot $r_{\rm crit}$, the minimum radius where fragmentation is allowed, for no dust settling ($h_d/h_g = 1$) in Figure 6-4. Figure 6-5 shows the case with partial dust settling ($h_d/h_g = 0.5$), and Figure 6-6 shows the case with significant dust settling ($h_d/h_g = 0.1$). Clearly, dust settling has a significant effect on the location of the minimum fragmentation radius. Note the slight spread due to the differing stellar luminosities arising as a result of age.

We can find Ω at $r_{\rm crit}$, $\Omega_{\rm crit}$, by simultaneously satisfying the conditions $\Omega_{\rm crit} t_{\rm cool} = 1$ and $Q = 1$ (eq. [1.1]). If we assume that $t_{\rm cool}$ is between the optically thick and self-heated limits, which have the same scalings (see eqs. [2.22] and [2.25]),

$$t_{\rm cool} \propto \frac{\chi^{\rm diff} \Sigma^2}{T_m^3} \ . \tag{6.1}$$

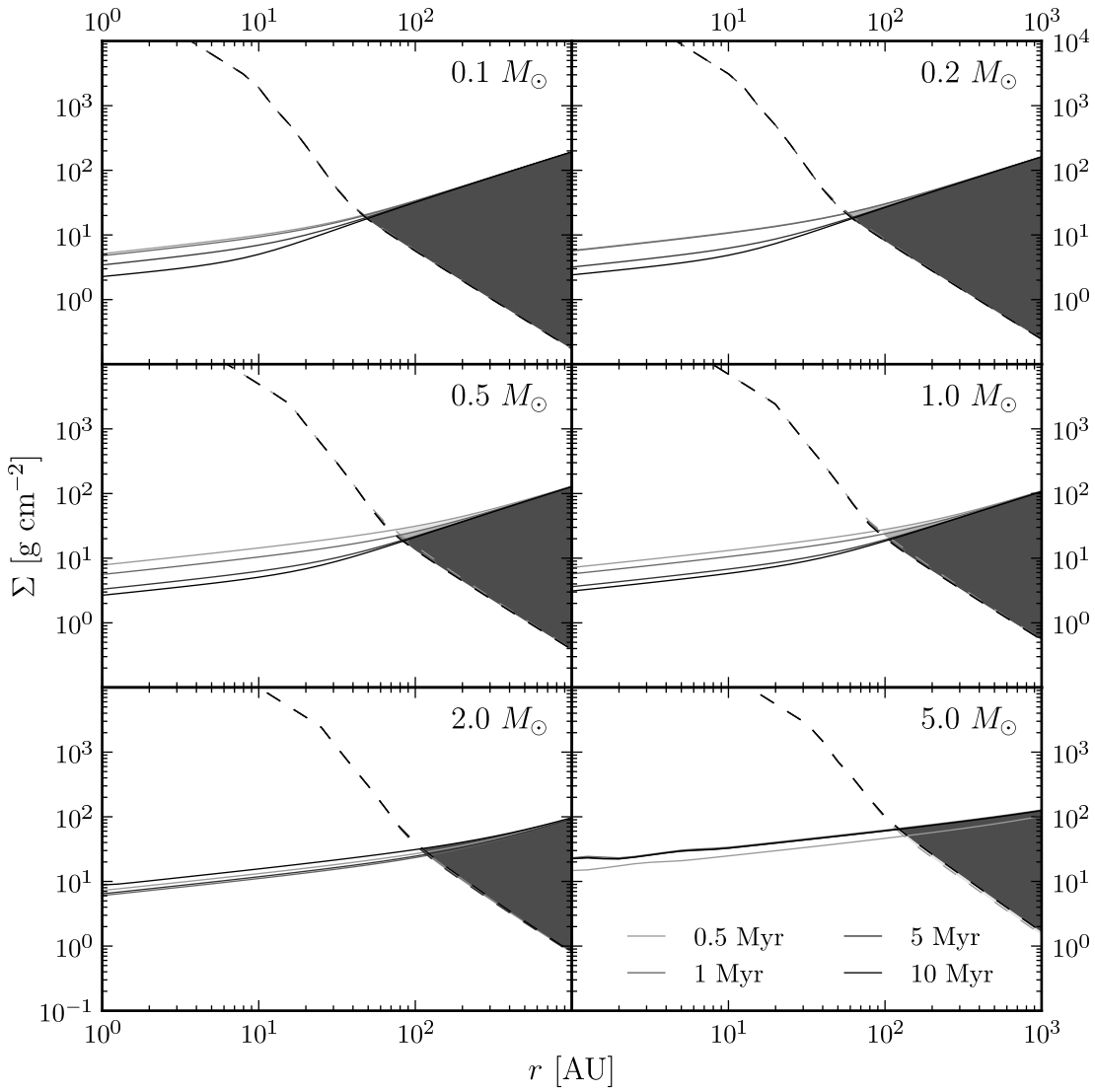

Figure 6-1: Surface density limits for disk fragmentation with no dust settling for 0.1, 0.2, 0.5, 1, 2, and 5 $M_\odot$ pre-main sequence stars. The solid lines denote the maximum surface density for fragmentation $\Sigma_{\rm max}$, while the dashed lines denotes the minimum surface density for fragmentation, $\Sigma_{\rm min}$. Disk fragmentation is only allowed in the region $\Sigma_{\rm max} > \Sigma_{\rm min}$, which is shaded gray. Light gray lines and shading correspond to a 0.5 Myr old pre-main sequence star, with increasingly darker gray lines and shading corresponding to 1, 5, and 10 Myr old pre-main sequence stars.

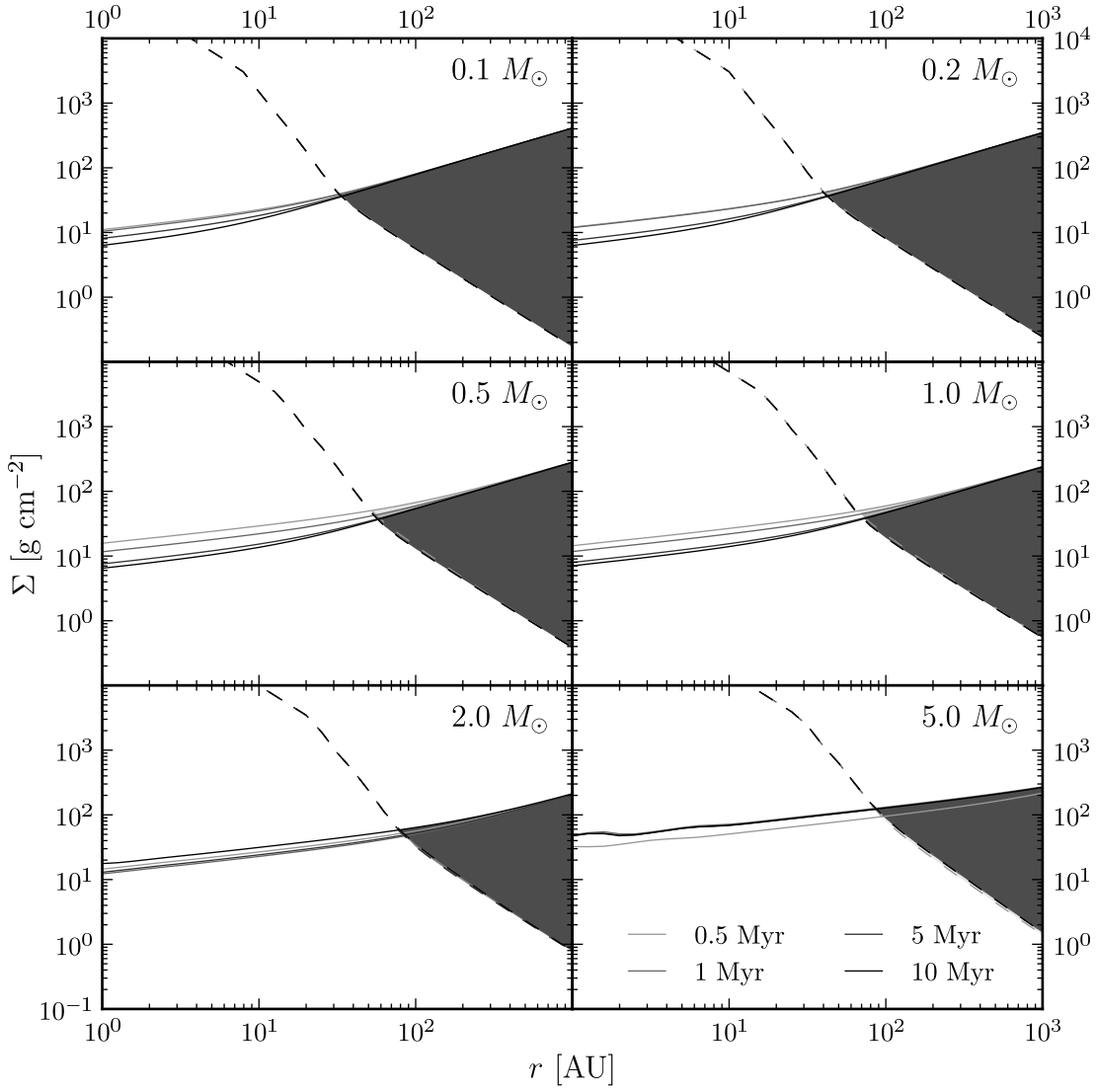

Figure 6-2: Same as Figure 6-1, but with $h_d/h_g = 0.5$, corresponding to partial dust settling.

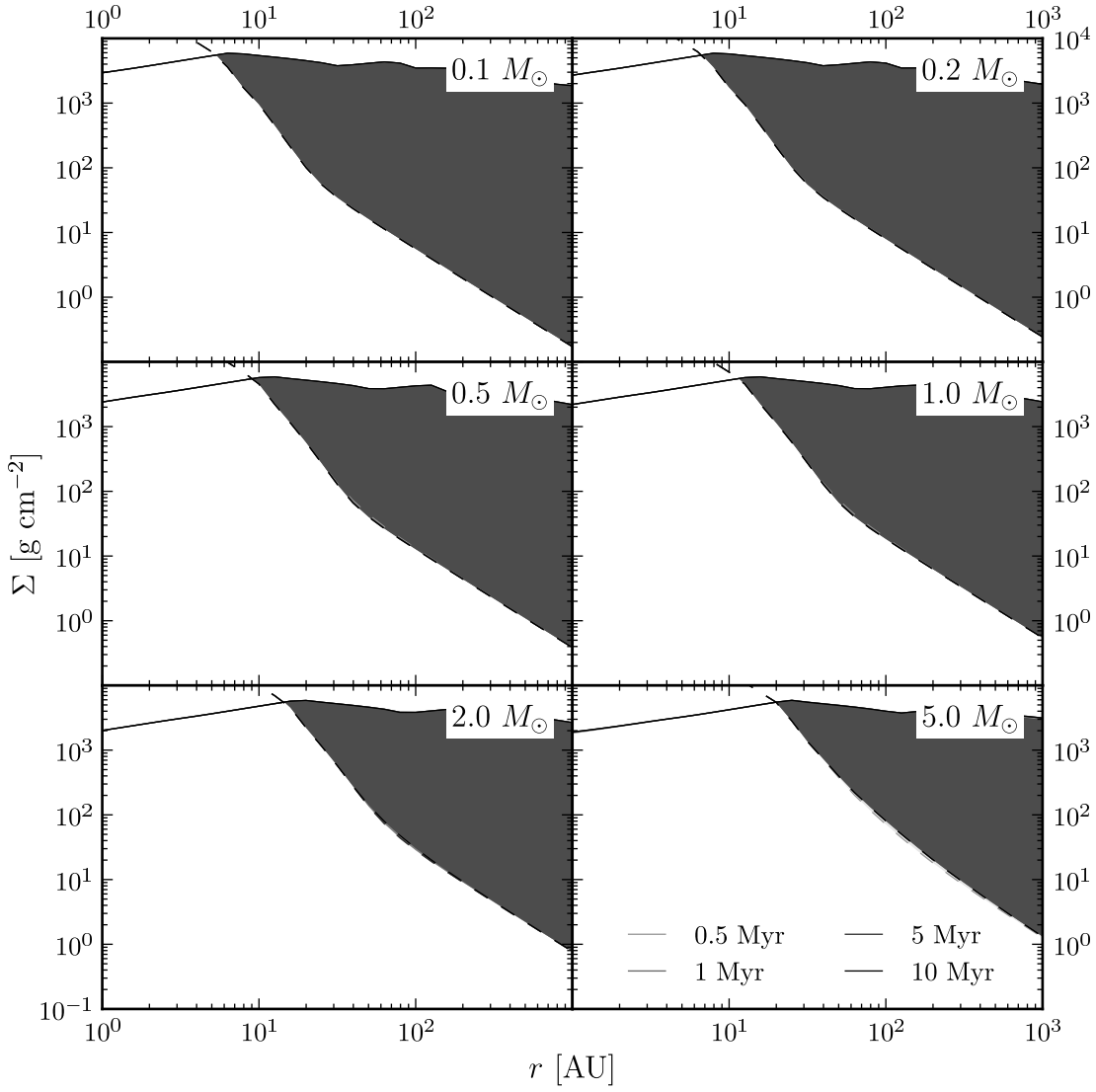

Figure 6-3: Same as Figure 6-1, but with $h_d/h_g = 0.1$, corresponding to significant dust settling.

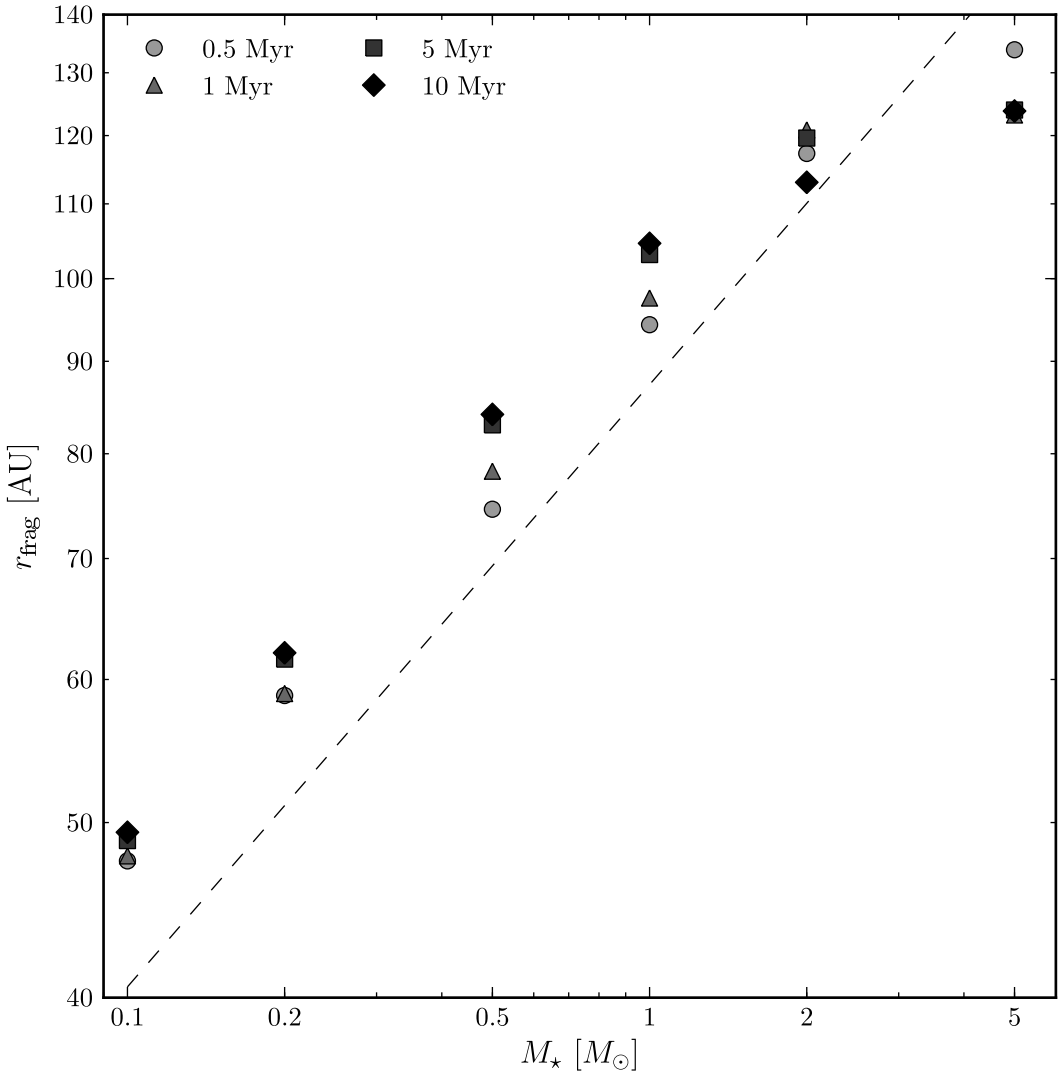

Figure 6-4: The minimum fragmentation radius as a function of protostellar mass and age, with no dust settling. The dashed line is the locus $r_{\rm frag} \propto M_\star^3$, which corresponds to the scaling of a Keplerian orbit with mass.

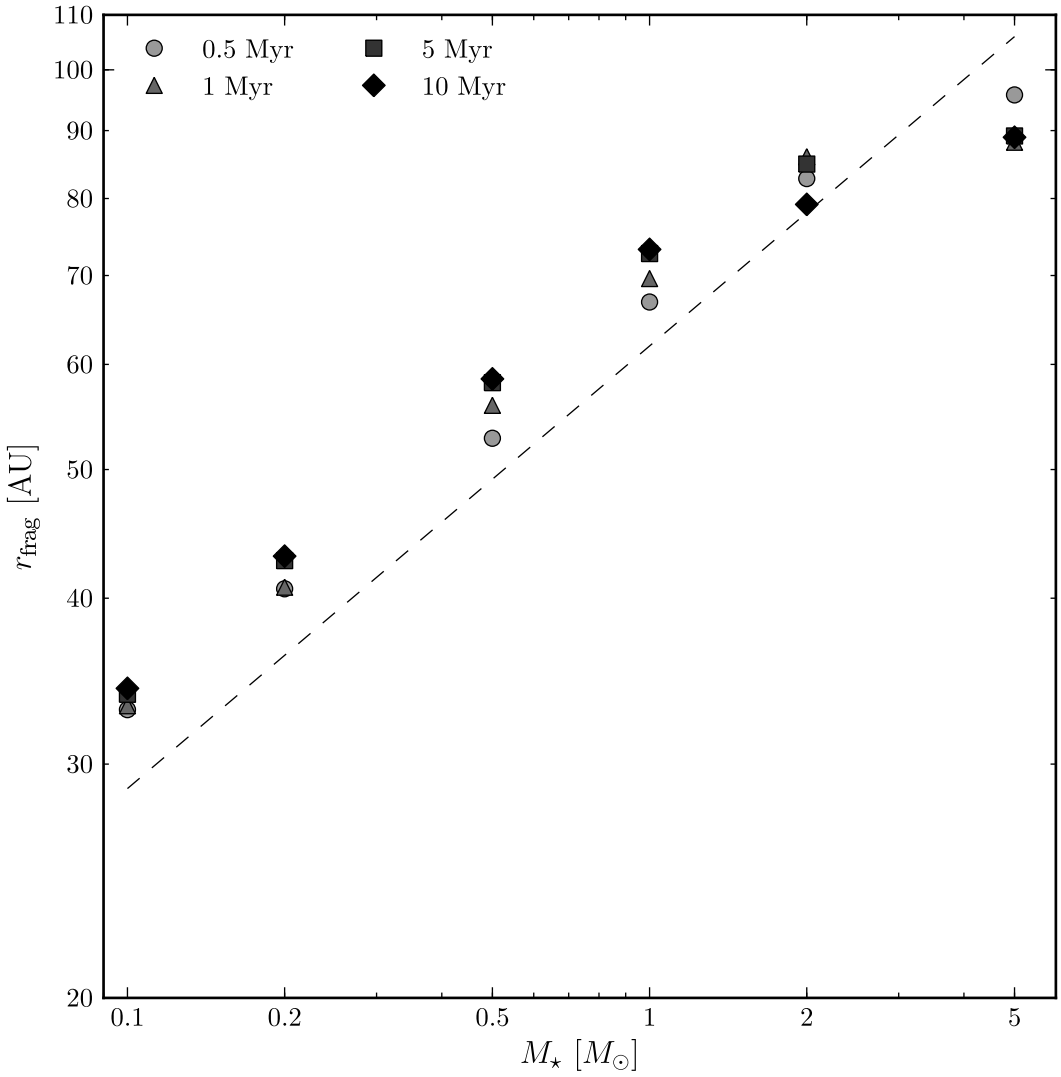

Figure 6-5: Same as Figure 6-4, but with $h_d/h_g = 0.5$, corresponding to partial dust settling.

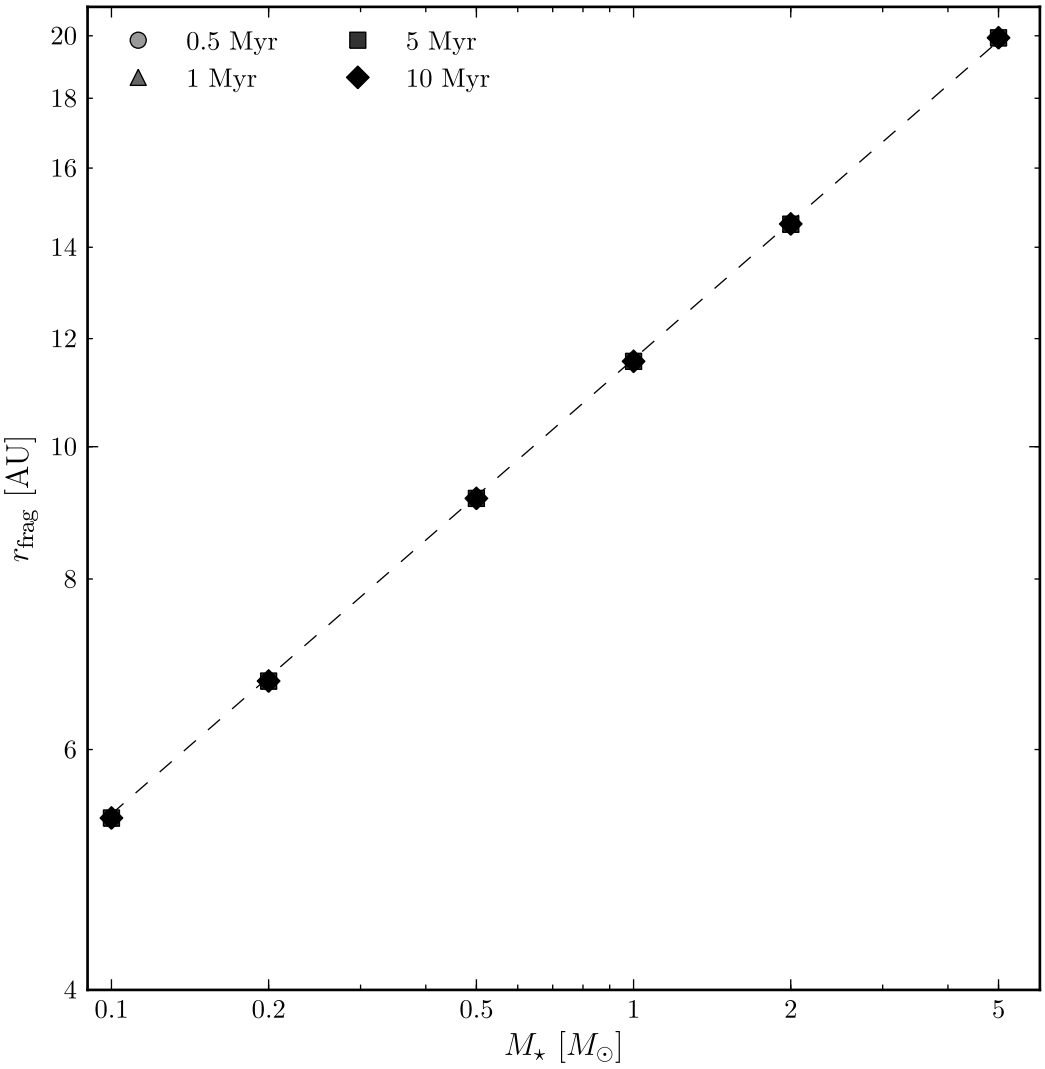

Figure 6-6: Same as Figure 6-4, but with $h_d/h_g = 0.1$, corresponding to significant dust settling.

Then, from the condition $Q = 1$, we find that $\Sigma^2 \propto \Omega_{\rm crit}^2 T_m$. Thus,

$$\Omega_{\rm crit} \propto \left(\frac{T_m^2}{\chi^{\rm diff}} \right)^{1/3} . \tag{6.2}$$

The opacity $\chi^{\rm diff}$ is a function of temperature, where $\chi^{\rm diff} \propto T$ for the dust model of Wood et al. (2002). We see that $\Omega_{\rm crit}$ is a constant that depends only weekly on mid-plane temperature.

Figures 6-4–6-6 also allow us to explore how $r_{\rm crit}$ scales with stellar mass. A good zeroth order approximation is to assume that $r_{\rm crit} \propto M^3$, corresponding to the scaling of a constant-period Keplerian orbit with mass (i.e. $\Omega_{\rm crit}$ is a constant independent of $M_\star$). However, we see that this assumption is only true when the perturbation cooling time becomes independent of the stellar illumination (i.e., for the case of significant dust settling where the stellar radiation is completely absorbed within the gas layers and the disk is strongly self-heated). In the cases of zero to partial dust settling, the stellar illumination is important, and $r_{\rm crit}$ has a somewhat more shallow slope. While this effect is limited to a $\sim 10\%$ error for low- to intermediate-mass stars, caution should be used when extrapolating to high-mass stars.

6.2 Range of Fragment Masses

Next, we explore the ranges of fragment mass expected to be produced by the parameter space covered in Figures 6-1–6-3. Using Equation (4.3), we plot the minimum fragmentation masses produced by 0.1, 0.2, 0.5, 1, 2, and 5 $M_\odot$ stars with ages 0.5, 1, 5, and 10 Myr and with no dust settling ($h_d/h_g = 1$) in Figure 6-7. The cases with partial dust settling ($h_d/h_g = 0.5$) and significant dust settling ($h_d/h_g = 0.1$) are shown in Figures 6-8 and 6-9, respectively. While the fragment masses shown here are only order-of-magnitude estimates, they can nonetheless help shed light on whether the disk fragmentation mechanism favors the formation of giant planets, brown dwarfs, or

binary stars. The obvious general trend is that lower mass stars produce lower mass fragments. Also of note is that while dust settling increases the range of radii where disk fragmentation is viable, it also slightly reduces the minimum fragment mass at a given radii. This later effect is due to the reduced mid-plane temperature caused by having less viscous energy generation occur within the optically thick dust layer. Nonetheless, it seems that disk fragmentation can only form giant planets for low- to intermediate-mass stars, with the more massive stars (i.e., $\gtrsim 5\,M_{\odot}$) forming brown dwarfs, and high-mass stars likely forming binaries. Also note that even if a fragment starts within the giant planet regime, it may proceed to accrete enough additional material to ultimately become a drown dwarf (Kratter et al., 2010).

Another interesting feature of Figure 6-9, is the sharp increase in fragment mass that occurs near the minimum fragmentation radius $r_{\rm crit}$. However, we point out that local surface densities of order 10^4 g cm^{-2} would be required for a disk to fragment under these conditions. While not impossible, such a large surface density could only come about as a result of significant local mass loading in the disk. Nonetheless, this provides a means by which low-mass stars can form surprisingly massive giant planets.

6.3 HR 8799 Revisited

Recall that we concluded in § 4.3 that HR 8799 c and d where unable to form at their current locations via disk fragmentation. However, Figure 6-3 indicates that it would, in fact, be possible for the disk to fragment at these radii, given significant dust settling ($h_d/h_g \approx 0.1$). However, we point out that fragmentation under these conditions would likely produce brown dwarfs rather than giant planets (see Figure 6-9). Thus, our conclusion remains that HR 8799 c and d likely did not form *in situ* through disk fragmentation.

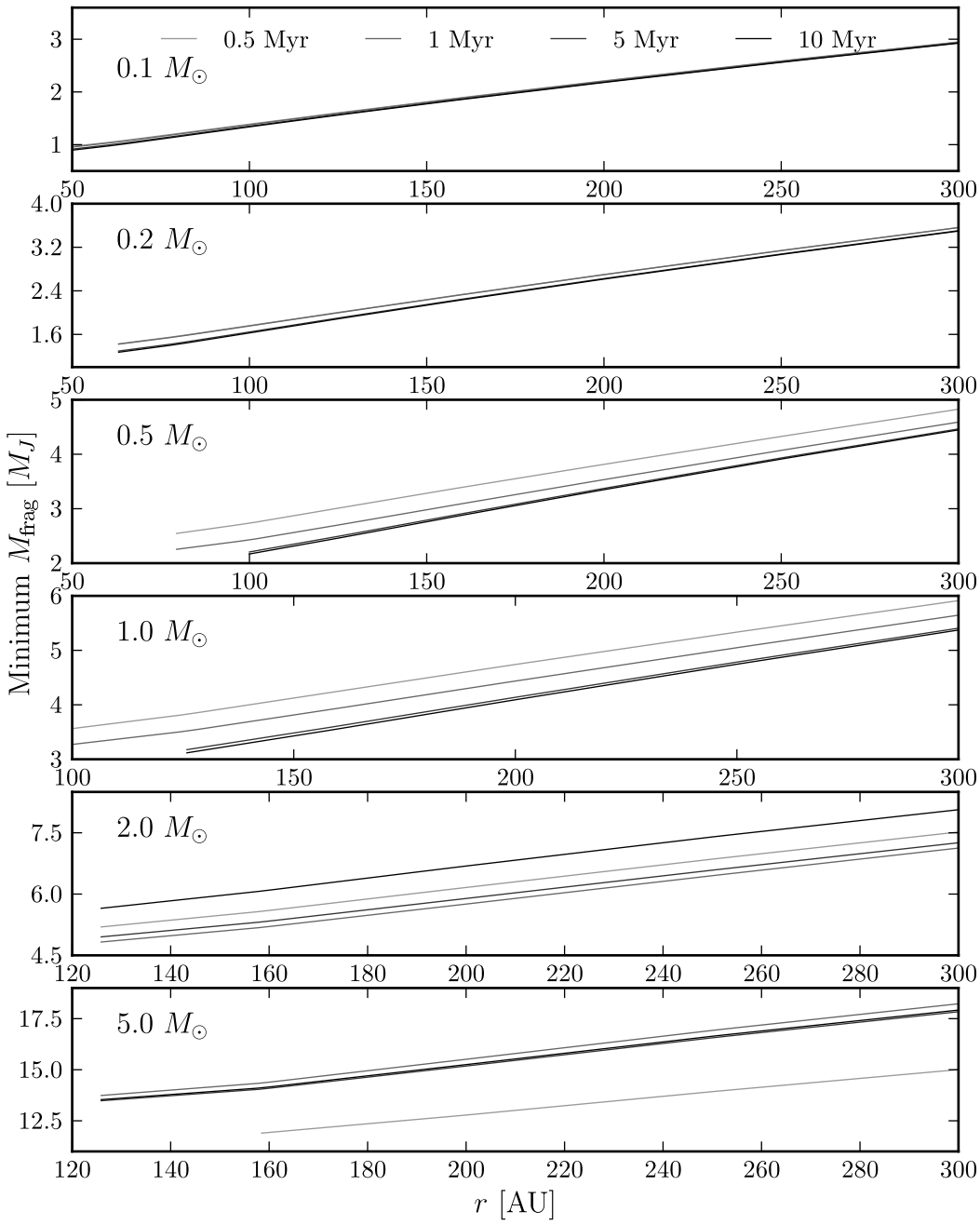

Figure 6-7: The minimum fragment mass as a function of distance, protostellar mass (0.1, 0.2, 0.5, 1, 2, and 5 $M_\odot$—shown top to bottom), and protostellar age (0.5, 1, 5, and 10 Myr—shown with lines of increasing dark shades of gray) with no dust settling.

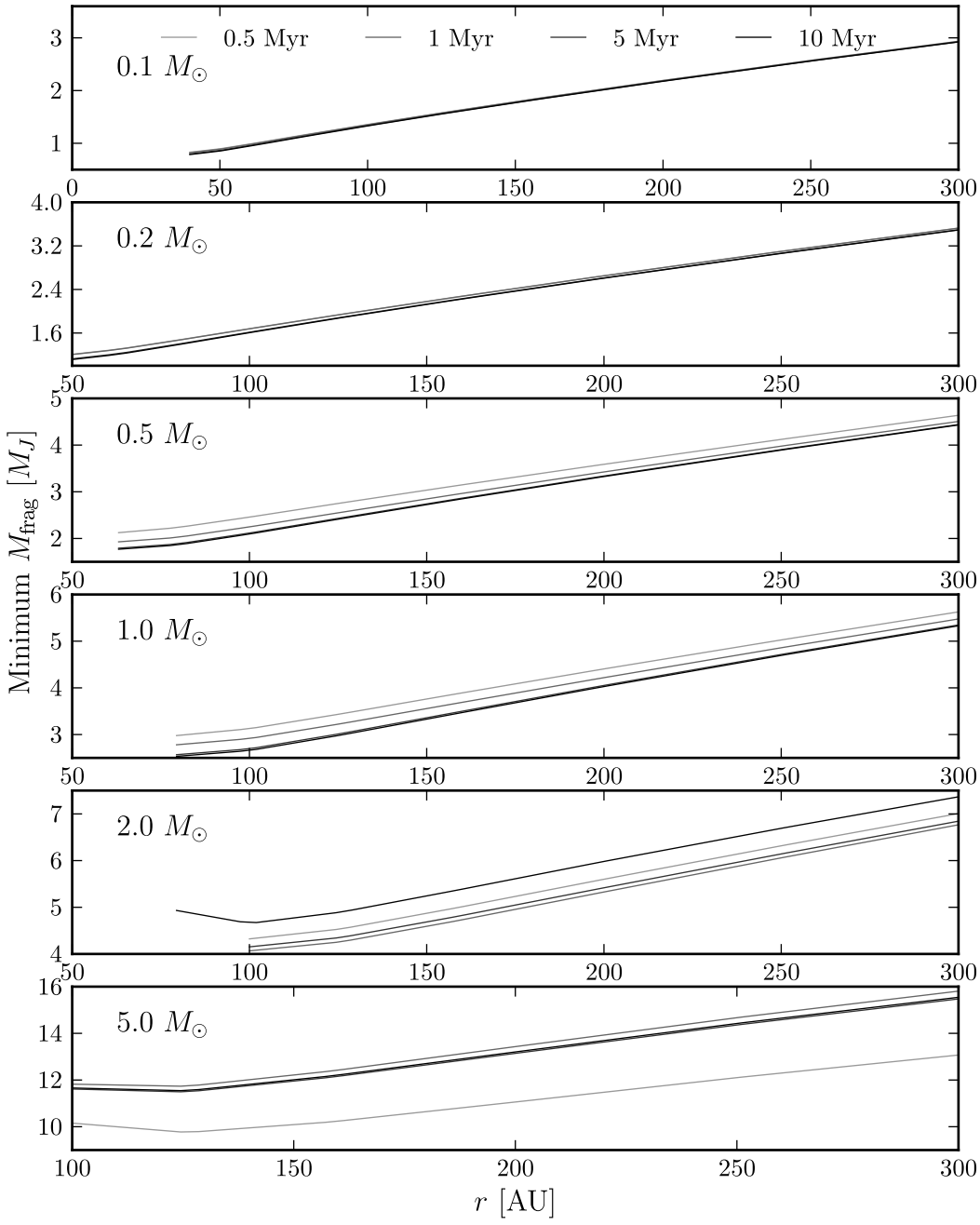

Figure 6-8: Same as Figure 6-7, but with $h_d/h_g = 0.5$, corresponding to partial dust settling.

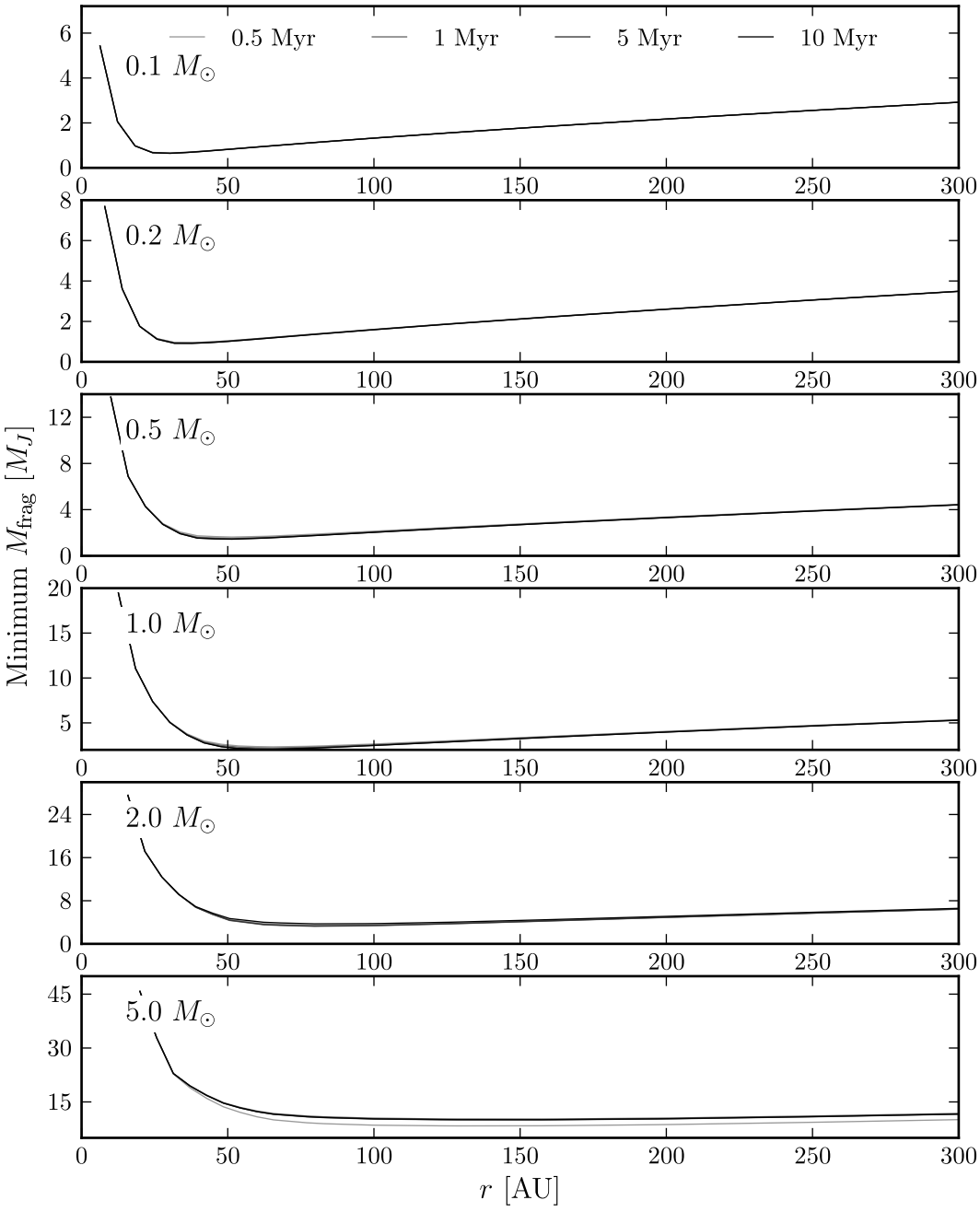

Figure 6-9: Same as Figure 6-7, but with $h_d/h_g = 0.1$, corresponding to significant dust settling.

Chapter 7

Summary

The primary topic of this thesis was the calculation of the cooling time for a point-like temperature perturbation in a circumstellar disk. This cooling time determines whether a Toomre $Q \lesssim 1$ disk is able to fragment, where the critical perturbation cooling time is given by $\Omega t_{\rm cool} \lesssim 1$.

To this end, we have developed an analytic technique for determining $t_{\rm cool}$ (eq. [2.20]). In addition, we have provided two useful analytic limits: Equation (2.21) for vertically isothermal disks (i.e., dominated by external illumination) and Equation (2.29) for self-heated disks (i.e., for significant viscous heating due to large surface density). We found that when self-heating dominates, the perturbation cooling time becomes a constant independent of opacity. For cases where $\xi\alpha \gtrsim 0.3$, a disk would satisfy the cooling criteria for fragmentation for all surface densities. When $\xi\alpha \lesssim 0.3$, the maximum surface density that satisfies the cooling criteria is set by Equation (2.21). An interesting consequence of this result occurs when gravitational turbulence is the primary source of viscosity (i.e. in a disk that is beginning to fragment). In this case, $\alpha \rightarrow 1$, and the cooling constraint remains satisfied for all surface densities. In other words, once a disk begins to fragment, it will keep fragmenting (as long as $Q \lesssim 1$).

To test the validity of our simplifications, we compared our analytic result with a

numerical Monte Carlo code, finding good agreement. The largest discrepancy occurs for intermediate optical depths where our assumption of constant Eddington factor begins to break down. Fortunately, since fragmentation is only likely to occur in a disk massive enough to be optically thick, this issue is minor.

We used these cooling times, along with the observed stellar parameters of Fomalhaut, HR 8799, and HL Tau, to test the viability of the disk fragmentation mechanism. We found that in each of these systems, at least one planet could have formed *in situ* as the result of fragmentation, assuming the disk mass interior to those planets fell within a particular range as indicated in Table 4.2.

While our initial cooling time calculations would appear to indicate that there is a maximum surface density above which fragmentation cannot occur, there are other effects that can decrease the cooling time. We considered two of these effects: 1) perturbations displaced from the disk mid-plane, and 2) dust settling toward the mid-plane. An expression for the perturbation cooling time including both of these effects was given in Equation (5.27). To account for these effects, along with the addition of uniform background illumination (i.e., from a surrounding 10 K cloud core), we modified our original one-layer model to include three layers: a central gas and settled dust layer surrounded on both sides by an optically thin, gray, pure gas layer (potentially of negligible size when there is no dust settling).

We showed that the effect of a vertically displaced perturbation tends to be limited to a factor of a few reduction in the perturbation cooling time, unless the perturbation is displaced by more than a scale height. The effect of dust settling, however, was much more pronounced. In particular, for $h_d/h_g \lesssim 0.1$, a disk will be below the critical cooling time for all realistic surface densities beyond the critical radius $r_{\rm crit}$ (with the exact required value for h_d/h_g depending on the value of $\xi\alpha$). In other words, with sufficient dust settling, $Q \lesssim 1$ becomes the only relevant requirement for disk fragmentation beyond the critical radius. Additionally, by combining a displaced

perturbation with dust settling, the critical value of h_d/h_g is reduced even further.

Next, we used our three-layer model to explore a range of stellar and disk parameters in order to show the effects of stellar age, mass, and degree of dust settling on the viability of disk fragmentation via the gravitational instability. We found that age has only a minor effect on the limits of disk fragmentation, particularly when the dust is well-settled.

In general, stellar mass serves to set the scale of the fragmentation region. However, the scaling is shallower than the typical zeroth order approximation indicates. Thus, care should be taken to extrapolate our results to high-mass stars.

While partial dust settling settling ($h_d/h_g = 0.5$) can move the critical fragmentation radius, $r_{\rm crit}$, inward by about 25%, significant dust settling ($h_d/h_g = 0.1$) moves the critical radius in by about an order of magnitude.

Finally, we used our technique for calculating fragment masses (eq. [4.3]) to investigate where the disk fragmentation mechanism forms giant planets versus brown dwarfs. Not surprisingly, low-mass stars are more likely to form giant planets while intermediate-mass stars are likely to form brown dwarfs (it follows that high-mass stars probably form binary companions). However, if the disk fragmentation occurs in the presence of dust settling, then slightly less-massive fragments are formed (by a factor of a few times 10%), except in the regions closest to $r_{\rm crit}$, where the fragment mass is greatly increased.

In conclusion, the gravitational instability remains a viable mechanism for the formation of giant planets: the perturbation cooling time can be sufficiently short to allow disk fragmentation over a range of realistic conditions, and geometrical effects, such as dust settling, further reduce the perturbation cooling time to the extent that cooling is sufficient for all realistic surface densities.

References

Alibert, Y., Mordasini, C., Benz, W., & Winisdoerffer, C. 2005, A&A, 434, 343

Andrews, S. M., & Williams, J. P. 2007, ApJ, 659, 705

Andriesse, C. D. 1977, Vistas in Astronomy, 21, 107

Bjorkman, J. E., & Wood, K. 2001, ApJ, 554, 615

Blum, J., & Wurm, G. 2008, ARA&A, 46, 21

Boss, A. P. 1997, Science, 276, 1836

Butler, R. P., et al. 2006, ApJ, 646, 505

Cameron, A. G. W. 1978, Moon and Planets, 18, 5

Chiang, E., Kite, E., Kalas, P., Graham, J. R., & Clampin, M. 2009, ApJ, 693, 734

Clarke, C. J., Harper-Clark, E., & Lodato, G. 2007, MNRAS, 381, 1543

Cotera, A. S., et al. 2001, ApJ, 556, 958

Durisen, R. H., Boss, A. P., Mayer, L., Nelson, A. F., Quinn, T., & Rice, W. K. M. 2007, Protostars and Planets V, 607

Gammie, C. F. 2001, ApJ, 553, 174

Greaves, J. S., Richards, A. M. S., Rice, W. K. M., & Muxlow, T. W. B. 2008, MNRAS, 391, L74

Haisch, K. E., Jr., Lada, E. A., & Lada, C. J. 2001, ApJ, 553, L153

Ikoma, M., Nakazawa, K., & Emori, H. 2000, ApJ, 537, 1013

Inaba, S., Wetherill, G. W., & Ikoma, M. 2003, Icarus, 166, 46

Kalas, P., et al. 2008, Science, 322, 1345

Kenyon, S. J., & Bromley, B. C. 2008, ApJS, 179, 451

Kenyon, S. J., & Hartmann, L. 1987, ApJ, 323, 714

Kratter, K. M., Murray-Clay, R. A., & Youdin, A. N. 2010, ApJ, 710, 1375

Kuiper, G. P. 1951, Proceedings of the National Academy of Science, 37, 1

Marois, C., Macintosh, B., Barman, T., Zuckerman, B., Song, I., Patience, J., Lafrenière, D., & Doyon, R. 2008, Science, 322, 1348

Mayor, M., & Queloz, D. 1995, Nature, 378, 355

Pollack, J. B., Hubickyj, O., Bodenheimer, P., Lissauer, J. J., Podolak, M., & Greenzweig, Y. 1996, Icarus, 124, 62

Rafikov, R. R. 2005, ApJ, 621, L69

Rice, W. K. M., Armitage, P. J., Bate, M. R., & Bonnell, I. A. 2003, MNRAS, 339, 1025

Shakura, N. I., & Sunyaev, R. A. 1973, A&A, 24, 337

Siess, L., Dufour, E., & Forestini, M. 2000, A&A, 358, 593

Stamatellos, D., & Whitworth, A. P. 2009, MNRAS, 392, 413

Toomre, A. 1964, ApJ, 139, 1217

Vorobyov, E. I. 2009, ApJ, 692, 1609

Vorobyov, E. I., & Basu, S. 2006, ApJ, 650, 956

Vorobyov, E. I., & Basu, S. 2009, MNRAS, 393, 822

Wood, K., Wolff, M. J., Bjorkman, J. E., & Whitney, B. 2002, ApJ, 564, 887

Zhu, Z., Hartmann, L., & Gammie, C. 2009, ApJ, 694, 1045

Appendix A

Boundary Conditions

A.1 One-Layer Model

In order to calculate the unknown constants $f^{\rm ext}$, $H_0^{\rm ext}$, $f^{\rm diff}$, and $g^{\rm diff}$ we utilize the boundary conditions

$$f^{\rm ext} = \frac{K_I^{\rm ext}(0)}{J_I^{\rm ext}(0)} , \tag{A.1}$$

$$H_0^{\rm ext} = H_I^{\rm ext}(\tau_0) , \tag{A.2}$$

$$f^{\rm diff} = \frac{K_I^{\rm diff}(0)}{J_I^{\rm diff}(0)} , \tag{A.3}$$

$$H^{\rm diff}(\tau_0) = H_I^{\rm diff}(\tau_0) , \tag{A.4}$$

respectively, where the I-subscript on the intensity moments indicates that they come from solving the transfer Equations (2.6) and (2.7), which are then used to calculate the moments J, H, and K. For simplicity, we assume that $f^{\rm ext}$ and $f^{\rm diff}$ are independent of depth. Note that while a seemingly more straight-forward alternative to Equation (A.4) is $g^{\rm diff} = H^{\rm diff}(\tau_0)/J^{\rm diff}(\tau_o)$, we have found that Equation (A.4) produces a more accurate solution, since $J^{\rm diff}(\tau_0)$ has a larger error arising from the assumption of constant Eddington factors than $H^{\rm diff}(\tau_0)$ does.

Using Equations (2.8) and (2.9) for the source functions $S^{\rm ext}$ and $S^{\rm diff}$, the intensity moments are

$$\begin{aligned} J_I^{\rm ext}(0) &= \frac{H_\star}{\mu_\star}\exp\left(-\frac{\tau_0^{\rm ext}}{\mu_\star}\right) + \int_0^{\tau_0^{\rm ext}} S^{\rm ext}(t)\ E_1(t)\,dt \\ &= \frac{H_\star}{\mu_\star}\exp\left(-\frac{\tau_0^{\rm ext}}{\mu_\star}\right) - \frac{\sigma^{\rm ext}}{\kappa^{\rm ext}}\frac{bH_0^{\rm ext}}{\sinh\beta\tau_0}\int_0^{\tau_0^{\rm ext}} \cosh bt\, E_1(t)\,dt\ , \end{aligned} \tag{A.5}$$

$$\begin{aligned} K_I^{\rm ext}(0) &= \mu_\star H_\star\exp\left(-\frac{\tau_0^{\rm ext}}{\mu_\star}\right) + \int_0^{\tau_0^{\rm ext}} S^{\rm ext}(t)\ E_3(t)\,dt \\ &= \mu_\star H_\star\exp\left(-\frac{\tau_0^{\rm ext}}{\mu_\star}\right) - \frac{\sigma^{\rm ext}}{\kappa^{\rm ext}}\frac{bH_0^{\rm ext}}{\sinh\beta\tau_0}\int_0^{\tau_0^{\rm ext}} \cosh bt\, E_3(t)\,dt\ , \end{aligned} \tag{A.6}$$

$$\begin{aligned} H_I^{\rm ext}(\tau_0) &= -\frac{H_\star}{2}\left(1-e^{-2\tau_0^{\rm ext}/\mu_\star}\right) + \frac{1}{2}\int_0^{2\tau_0^{\rm ext}} S^{\rm ext}\left(\tau_0^{\rm ext}-t\right)\ E_2(t)\,dt \\ &= -\frac{H_\star}{2}\left(1-e^{-2\tau_0^{\rm ext}/\mu_\star}\right) \\ &\quad -\frac{1}{2}\frac{\sigma^{\rm ext}}{\kappa^{\rm ext}}\frac{bH_0^{\rm ext}}{\sinh\beta\tau_0}\int_0^{2\tau_0^{\rm ext}} \cosh b(\tau_0^{\rm ext}-t)\, E_2(t)\,dt\ , \end{aligned} \tag{A.7}$$

and

$$\begin{aligned} J_I^{\rm diff}(0) &= \int_0^{\tau_0} S^{\rm diff}(t)\ E_1(t)\,dt \\ &= \left[H_0\left(\frac{1}{g^{\rm diff}}+\frac{\tau_0}{2f^{\rm diff}}+\frac{1}{\tau_0}\right)\right. \\ &\quad \left. -H_0^{\rm ext}\left(\frac{1}{g^{\rm diff}}+\frac{1}{\beta f^{\rm diff}}\frac{\cosh\beta\tau_0}{\sinh\beta\tau_0}\right)\right]\int_0^{\tau_0} E_1(t)\,dt \\ &\quad -\frac{H_0}{2f^{\rm diff}\tau_0}\int_0^{\tau_0} t^2\, E_1(t)\,dt \\ &\quad -\left(\beta-\frac{1}{\beta f^{\rm diff}}\right)\frac{H_0^{\rm ext}}{\sinh\beta\tau_0}\int_0^{\tau_0}\cosh\beta t\, E_1(t)\,dt\ , \end{aligned} \tag{A.8}$$

$$
\begin{aligned}
K_I^{\rm diff}(0) &= \int_0^{\tau_0} S^{\rm diff}\,(t)\;E_3(t)\,dt \\
&= \left[H_0\left(\frac{1}{g^{\rm diff}}+\frac{\tau_0}{2f^{\rm diff}}+\frac{1}{\tau_0}\right)\right. \\
&\quad \left. -H_0^{\rm ext}\left(\frac{1}{g^{\rm diff}}+\frac{1}{\beta f^{\rm diff}}\frac{\cosh\beta\tau_0}{\sinh\beta\tau_0}\right)\right]\int_0^{\tau_0} E_3(t)\,dt \\
&\quad -\frac{H_0}{2f^{\rm diff}\tau_0}\int_0^{\tau_0} t^2\,E_3(t)\,dt \\
&\quad -\left(\beta-\frac{1}{\beta f^{\rm diff}}\right)\frac{H_0^{\rm ext}}{\sinh\beta\tau_0}\int_0^{\tau_0}\cosh\beta t\,E_3(t)\,dt\;, \qquad \text{(A.9)}
\end{aligned}
$$

$$
\begin{aligned}
H_I^{\rm diff}(\tau_0) &= \frac{1}{2}\int_0^{2\tau_0} S^{\rm diff}\,(\tau_0-t)\;E_2(t)\,dt \\
&= \frac{1}{2}\left[H_0\left(\frac{1}{g^{\rm diff}}+\frac{1}{\tau_0}\right)\right. \\
&\quad \left. -H_0^{\rm ext}\left(\frac{1}{g^{\rm diff}}+\frac{1}{\beta f^{\rm diff}}\frac{\cosh\beta\tau_0}{\sinh\beta\tau_0}\right)\right]\int_0^{2\tau_0} E_2(t)\,dt \\
&\quad +\frac{H_0}{2f^{\rm diff}}\int_0^{2\tau_0} t\,E_2(t)\,dt-\frac{H_0}{4f\tau_0}\int_0^{2\tau_0} t^2\,E_2(t)\,dt \\
&\quad -\frac{1}{2}\left(\beta-\frac{1}{\beta f^{\rm diff}}\right)\frac{H_0^{\rm ext}}{\sinh\beta\tau_0} \\
&\quad \cdot\int_0^{2\tau_0}\cosh\beta(\tau_0-t)\,E_2(t)\,dt\;, \qquad \text{(A.10)}
\end{aligned}
$$

where E_1, E_2, and E_3 are exponential integrals, $\tau_0^{\rm ext} = (\chi^{\rm ext}/\chi^{\rm diff})\tau_0$, and $b = (\chi^{\rm diff}/\chi^{\rm ext})\beta$. Note that all of the above integrals involving E_1, E_2, and E_3 can be solved analytically (see Appendix B). The Eddington flux from the star incident on the disk is

$$
H_\star = \frac{\mu_\star}{4\pi}\left(\frac{R_\star}{r}\right)^2\sigma T_\star^4 \qquad \text{(A.11)}
$$

where $\mu_\star$ is the cosine of the angle between the disk normal and the star, and $R_\star$ and $T_\star$ are the stellar radius and effective temperature.

To find $f^{\rm ext}$, $H_0^{\rm ext}$, $f^{\rm diff}$, and $g^{\rm diff}$, we assume starting values of $\mu_\star^2$, $-H_\star/2$, 1/3, and 1/2, respectively. We then evaluate Equations (A.1)–(A.4) analytically and iterate until convergence. For temperature-dependent quantities (i.e. opacity), we use the mid-plane temperature, which is also calculated iteratively.

A.2 Three-Layer Model

In the three-layer model described in § 5.2, the *external* radiation field is split into three components: direct stellar irradiation, radiation from the two optically thin gas layers, and 10 K background radiation. The *star* intensity moments are

$$J_I^{\rm star}(0) = \frac{H_\star}{\mu_\star}\exp\left(-\frac{\tau_0^{\rm star}+\tau_g}{\mu_\star}\right) - \frac{\sigma^{\rm star}}{\kappa^{\rm star}}\frac{b^{\rm star}H_0^{\rm star}}{\sinh\beta^{\rm star}\tau_0}\int_0^{\tau_0^{\rm star}}\cosh b^{\rm star}t\,E_1(t)\,dt\ , \tag{A.12}$$

$$K_I^{\rm star}(0) = \mu_\star H_\star\exp\left(-\frac{\tau_0^{\rm star}+\tau_g}{\mu_\star}\right) - \frac{\sigma^{\rm star}}{\kappa^{\rm star}}\frac{b^{\rm star}H_0^{\rm star}}{\sinh\beta^{\rm star}\tau_0}\int_0^{\tau_0^{\rm star}}\cosh b^{\rm star}t\,E_3(t)\,dt\ , \tag{A.13}$$

$$H_I^{\rm star}(\tau_0) = -\frac{H_\star}{2}\left(1-e^{-2\tau_0^{\rm star}/\mu_\star}\right)e^{-\tau_g/\mu_\star} - \frac{1}{2}\frac{\sigma^{\rm star}}{\kappa^{\rm star}}\frac{b^{\rm star}H_0^{\rm star}}{\sinh\beta^{\rm star}\tau_0} \times\int_0^{2\tau_0^{\rm star}}\cosh b^{\rm star}(\tau_0^{\rm star}-t)\,E_2(t)\,dt\ , \tag{A.14}$$

where $\tau_0^{\rm star} = (\chi^{\rm star}/\chi^{\rm diff})\tau_0$ and $b^{\rm star} = (\chi^{\rm diff}/\chi^{\rm star})\beta^{\rm star}$. The *surface* intensity moments are

$$J_I^{\rm surf}(0) = S^{\rm gas}\left[E_2(\tau_0^{\rm surf}) - E_2(\tau_0^{\rm surf}+\tau_g)\right] - \frac{\sigma^{\rm surf}}{\kappa^{\rm surf}}\frac{b^{\rm surf}H_0^{\rm surf}}{\sinh\beta^{\rm surf}\tau_0}\int_0^{\tau_0^{\rm surf}}\cosh b^{\rm surf}t\,E_1(t)\,dt\ , \tag{A.15}$$

$$K_I^{\rm surf}(0) = S^{\rm gas}\left[E_4(\tau_0^{\rm surf}) - E_4(\tau_0^{\rm surf}+\tau_g)\right] - \frac{\sigma^{\rm surf}}{\kappa^{\rm surf}}\frac{b^{\rm surf}H_0^{\rm surf}}{\sinh\beta^{\rm surf}\tau_0}\int_0^{\tau_0^{\rm surf}}\cosh b^{\rm surf}t\,E_3(t)\,dt\ , \tag{A.16}$$

$$H_I^{\rm surf}(\tau_0) = \frac{S^{\rm gas}}{2}\left[-\frac{1}{2}+E_3(\tau_g)+E_3(2\tau_0^{\rm surf})-E_3(2\tau_0^{\rm surf}+\tau_g)\right] - \frac{1}{2}\frac{\sigma^{\rm surf}}{\kappa^{\rm surf}}\frac{b^{\rm surf}H_0^{\rm surf}}{\sinh\beta^{\rm surf}\tau_0} \times\int_0^{2\tau_0^{\rm surf}}\cosh b^{\rm surf}(\tau_0^{\rm surf}-t)\,E_2(t)\,dt\ , \tag{A.17}$$

where $\tau_0^{\rm surf} = (\chi^{\rm surf}/\chi^{\rm diff})\tau_0$, $b^{\rm surf} = (\chi^{\rm diff}/\chi^{\rm surf})\beta^{\rm surf}$, and

$$S^{\rm gas} = \frac{H_\star}{2\mu_\star}\left[1+\exp\left(-\frac{2\tau_0+\tau_g}{\mu_\star}\right)\right]+\frac{\sigma T^4}{2\pi}\left[1+E_2(2\tau_0+\tau_g)\right] + \frac{H_0-H_0^{\rm star}-H_0^{\rm surf}-H_0^{\rm bg}}{g^{\rm diff}}+\frac{H_g}{\tau_g}\ . \tag{A.18}$$

The *background* intensity moments are

$$J_I^{\rm bg}(0) = \frac{\sigma T_{\rm bg}^4}{\pi}E_2(\tau_0^{\rm bg}+\tau_g) - \frac{\sigma^{\rm bg}}{\kappa^{\rm bg}}\frac{b^{\rm bg}H_0^{\rm bg}}{\sinh\beta^{\rm bg}\tau_0}\int_0^{\tau_0^{\rm bg}}\cosh b^{\rm bg}t\,E_1(t)\,dt\ , \tag{A.19}$$

$$K_I^{\rm bg}(0) = \frac{\sigma T_{\rm bg}^4}{\pi} E_4(\tau_0^{\rm bg} + \tau_g) - \frac{\sigma^{\rm bg}}{\kappa^{\rm bg}} \frac{b^{\rm bg} H_0^{\rm bg}}{\sinh \beta^{\rm bg} \tau_0} \int_0^{\tau_0^{\rm bg}} \cosh b^{\rm bg} t \, E_3(t) \, dt \ , \qquad \text{(A.20)}$$

$$H_I^{\rm bg}(\tau_0) = \frac{\sigma T_{\rm bg}^4}{2\pi} \left[-E_3(\tau_g) + E_3(2\tau_0^{\rm bg} + \tau_g) \right] - \frac{1}{2} \frac{\sigma^{\rm bg}}{\kappa^{\rm bg}} \frac{b^{\rm bg} H_0^{\rm bg}}{\sinh \beta^{\rm bg} \tau_0} \int_0^{2\tau_0^{\rm bg}} \cosh b^{\rm bg} (\tau_0^{\rm bg} - t) \, E_2(t) \, dt \ , \qquad \text{(A.21)}$$

where $\tau_0^{\rm bg} = (\chi^{\rm bg}/\chi^{\rm diff})\tau_0$ and $b^{\rm bg} = (\chi^{\rm diff}/\chi^{\rm bg})\beta^{\rm bg}$.

The *diffuse* intensity moments are now modified by the addition of the two gas layers and the *background* radiation field. The modified *diffuse* intensity moments are

$$\begin{aligned} J_I^{\rm diff}(0) = {} & H_0 \left(\frac{1}{g^{\rm diff}} + \frac{\tau_0}{2 f^{\rm diff}} + \frac{1}{\tau_0} \right) \int_0^{\tau_0} E_1(t) \, dt \\ & - \frac{H_0}{2 f^{\rm diff} \tau_0} \int_0^{\tau_0} t^2 \, E_1(t) \, dt \\ & - H_0^{\rm star} \left(\frac{1}{g^{\rm diff}} + \frac{1}{\beta^{\rm star} f^{\rm diff}} \frac{\cosh \beta^{\rm star} \tau_0}{\sinh \beta^{\rm star} \tau_0} \right) \int_0^{\tau_0} E_1(t) \, dt \\ & - \left(\beta^{\rm star} - \frac{1}{\beta^{\rm star} f^{\rm diff}} \right) \frac{H_0^{\rm star}}{\sinh \beta^{\rm star} \tau_0} \int_0^{\tau_0} \cosh \beta^{\rm star} t \, E_1(t) \, dt \\ & - H_0^{\rm surf} \left(\frac{1}{g^{\rm diff}} + \frac{1}{\beta^{\rm surf} f^{\rm diff}} \frac{\cosh \beta^{\rm surf} \tau_0}{\sinh \beta^{\rm surf} \tau_0} \right) \int_0^{\tau_0} E_1(t) \, dt \\ & - \left(\beta^{\rm surf} - \frac{1}{\beta^{\rm surf} f^{\rm diff}} \right) \frac{H_0^{\rm surf}}{\sinh \beta^{\rm surf} \tau_0} \int_0^{\tau_0} \cosh \beta^{\rm surf} t \, E_1(t) \, dt \\ & - H_0^{\rm bg} \left(\frac{1}{g^{\rm diff}} + \frac{1}{\beta^{\rm bg} f^{\rm diff}} \frac{\cosh \beta^{\rm bg} \tau_0}{\sinh \beta^{\rm bg} \tau_0} \right) \int_0^{\tau_0} E_1(t) \, dt \\ & - \left(\beta^{\rm bg} - \frac{1}{\beta^{\rm bg} f^{\rm diff}} \right) \frac{H_0^{\rm bg}}{\sinh \beta^{\rm bg} \tau_0} \int_0^{\tau_0} \cosh \beta^{\rm bg} t \, E_1(t) \, dt \ , \end{aligned} \qquad \text{(A.22)}$$

$$
\begin{aligned}
K_I^{\rm diff}(0) &= H_0 \left(\frac{1}{g^{\rm diff}} + \frac{\tau_0}{2f^{\rm diff}} + \frac{1}{\tau_0} \right) \int_0^{\tau_0} E_3(t)\, dt \\
&\quad - \frac{H_0}{2f^{\rm diff}\tau_0} \int_0^{\tau_0} t^2\, E_3(t)\, dt \\
&\quad - H_0^{\rm star} \left(\frac{1}{g^{\rm diff}} + \frac{1}{\beta^{\rm star} f^{\rm diff}} \frac{\cosh \beta^{\rm star}\tau_0}{\sinh \beta^{\rm star}\tau_0} \right) \int_0^{\tau_0} E_3(t)\, dt \\
&\quad - \left(\beta^{\rm star} - \frac{1}{\beta^{\rm star} f^{\rm diff}} \right) \frac{H_0^{\rm star}}{\sinh \beta^{\rm star}\tau_0} \int_0^{\tau_0} \cosh \beta^{\rm star} t\, E_3(t)\, dt \\
&\quad - H_0^{\rm surf} \left(\frac{1}{g^{\rm diff}} + \frac{1}{\beta^{\rm surf} f^{\rm diff}} \frac{\cosh \beta^{\rm surf}\tau_0}{\sinh \beta^{\rm surf}\tau_0} \right) \int_0^{\tau_0} E_3(t)\, dt \\
&\quad - \left(\beta^{\rm surf} - \frac{1}{\beta^{\rm surf} f^{\rm diff}} \right) \frac{H_0^{\rm surf}}{\sinh \beta^{\rm surf}\tau_0} \int_0^{\tau_0} \cosh \beta^{\rm surf} t\, E_3(t)\, dt \\
&\quad - H_0^{\rm bg} \left(\frac{1}{g^{\rm diff}} + \frac{1}{\beta^{\rm bg} f^{\rm diff}} \frac{\cosh \beta^{\rm bg}\tau_0}{\sinh \beta^{\rm bg}\tau_0} \right) \int_0^{\tau_0} E_3(t)\, dt \\
&\quad - \left(\beta^{\rm bg} - \frac{1}{\beta^{\rm bg} f^{\rm diff}} \right) \frac{H_0^{\rm bg}}{\sinh \beta^{\rm bg}\tau_0} \int_0^{\tau_0} \cosh \beta^{\rm bg} t\, E_3(t)\, dt \ , \qquad \text{(A.23)}
\end{aligned}
$$

$$
\begin{aligned}
H_I^{\rm diff}(\tau_0) &= \frac{1}{2} H_0 \left(\frac{1}{g^{\rm diff}} + \frac{1}{\tau_0} \right) \int_0^{2\tau_0} E_2(t)\, dt \\
&\quad + \frac{H_0}{2f^{\rm diff}} \int_0^{2\tau_0} t\, E_2(t)\, dt - \frac{H_0}{4f\tau_0} \int_0^{2\tau_0} t^2\, E_2(t)\, dt \\
&\quad - \frac{H_0^{\rm star}}{2} \left(\frac{1}{g^{\rm diff}} + \frac{1}{\beta^{\rm star} f^{\rm diff}} \frac{\cosh \beta^{\rm star}\tau_0}{\sinh \beta^{\rm star}\tau_0} \right) \int_0^{2\tau_0} E_2(t)\, dt \\
&\quad - \frac{1}{2} \left(\beta^{\rm star} - \frac{1}{\beta^{\rm star} f^{\rm diff}} \right) \frac{H_0^{\rm star}}{\sinh \beta^{\rm star}\tau_0} \int_0^{2\tau_0} \cosh \beta^{\rm star}(\tau_0 - t)\, E_2(t)\, dt \\
&\quad - \frac{H_0^{\rm surf}}{2} \left(\frac{1}{g^{\rm diff}} + \frac{1}{\beta^{\rm surf} f^{\rm diff}} \frac{\cosh \beta^{\rm surf}\tau_0}{\sinh \beta^{\rm surf}\tau_0} \right) \int_0^{2\tau_0} E_2(t)\, dt \\
&\quad - \frac{1}{2} \left(\beta^{\rm surf} - \frac{1}{\beta^{\rm surf} f^{\rm diff}} \right) \frac{H_0^{\rm surf}}{\sinh \beta^{\rm surf}\tau_0} \int_0^{2\tau_0} \cosh \beta^{\rm surf}(\tau_0 - t)\, E_2(t)\, dt \\
&\quad - \frac{H_0^{\rm bg}}{2} \left(\frac{1}{g^{\rm diff}} + \frac{1}{\beta^{\rm bg} f^{\rm diff}} \frac{\cosh \beta^{\rm bg}\tau_0}{\sinh \beta^{\rm bg}\tau_0} \right) \int_0^{2\tau_0} E_2(t)\, dt \\
&\quad - \frac{1}{2} \left(\beta^{\rm bg} - \frac{1}{\beta^{\rm bg} f^{\rm diff}} \right) \frac{H_0^{\rm bg}}{\sinh \beta^{\rm bg}\tau_0} \\
&\quad \times \int_0^{2\tau_0} \cosh \beta^{\rm bg}(\tau_0 - t)\, E_2(t)\, dt \ . \qquad \text{(A.24)}
\end{aligned}
$$

Appendix B

Integrals Involving E_1, E_2, and E_3

B.1 Integrals Involving E_1

$$\int_0^x E_1(t)\,dt = 1 - E_2(x) \tag{B.1}$$

$$\int_0^x t^2 E_1(t)\,dt = \frac{2}{3} - 2E_4(x) - 2xE_3(x) - x^2E_2(x) \tag{B.2}$$

$$\begin{aligned}\int_0^x \cosh at\, E_1(t)\,dt &= \frac{\sinh ax}{a}E_1(x) \\ &\quad + \frac{E_1[(1+a)x] - E_1[(1-a)x] + \ln\left(\frac{1+a}{1-a}\right)}{2a}\end{aligned} \tag{B.3}$$

B.2 Integrals Involving E_2

$$\int_0^x E_2(t)\,dt = \frac{1}{2} - E_3(x) \tag{B.4}$$

$$\int_0^x tE_2(t)\,dt = \frac{1}{3} - E_4(x) - xE_3(x) \tag{B.5}$$

$$\int_0^x t^2E_2(t)\,dt = \frac{1}{2} - 2E_5(x) - 2xE_4(x) - x^2E_3(x) \tag{B.6}$$

$$\begin{aligned}\int_0^x \cosh at\, E_2(t)\,dt &= \frac{\sinh ax}{a}E_2(x) + \frac{\cosh ax}{a^2}E_1(x) \\ &\quad - \frac{E_1[(1+a)x] + E_1[(1-a)x] + \ln(1-a^2)}{2a^2}\end{aligned} \tag{B.7}$$

$$\begin{aligned}\int_0^{2x} \cosh a(x-t)\, E_2(t)\,dt &= \frac{\sinh ax}{a}E_2(2x) + \frac{\sinh ax}{a} + \frac{\cosh ax}{a^2}E_1(2x) \\ &\quad - e^{ax}\left(\frac{E_1[2(1+a)x] + \ln(1+a)}{2a^2}\right) \\ &\quad - e^{-ax}\left(\frac{E_1[2(1-a)x] + \ln(1-a)}{2a^2}\right)\end{aligned} \tag{B.8}$$

B.3 Integrals Involving E_3

$$\int_0^x E_3(t)\,dt = \frac{1}{3} - E_4(x) \tag{B.9}$$

$$\int_0^x tE_3(t)\,dt = \frac{1}{4} - E_5(x) - xE_4(x) \tag{B.10}$$

$$\int_0^x t^2E_3(t)\,dt = \frac{2}{5} - 2E_6(x) - 2xE_5(x) - x^2E_4(x) \tag{B.11}$$

$$\int_0^x \cosh at\, E_3(t)\, dt = \frac{\sinh ax}{a} E_3(x) + \frac{\cosh ax}{a^2} E_2(x) + \frac{\sinh ax}{a^3} E_1(x) - \frac{1}{a^2} + \frac{E_1[(1+a)x] - E_1[(1-a)x] + \ln\left(\frac{1+a}{1-a}\right)}{2a^3} \tag{B.12}$$